

Subnanometer localization accuracy in widefield optical microscopy

Craig R. Copeland^{1,2}, Craig D. McGray³, Jon Geist³, Vladimir A. Aksyuk¹, J. Alexander Liddle¹, B. Robert Ilic¹, and Samuel M. Stavis^{1,*}

¹Center for Nanoscale Science and Technology, National Institute of Standards and Technology, Gaithersburg, Maryland 20899, United States of America, ²Maryland Nanocenter, University of Maryland, College Park, Maryland 20742, United States of America, ³Engineering Physics Division, National Institute of Standards and Technology, Gaithersburg, Maryland 20899, United States of America

The common assumption that localization precision is the limit of localization accuracy and the typical absence of comprehensive calibration of optical microscopes present a widespread problem in localization microscopy. This combination causes overconfidence in measurement results with statistical uncertainties at the nanometer scale that are invalid due to systematic errors that can be orders of magnitude larger. In this article, we report a comprehensive solution to this underappreciated problem of false precision. We fabricate and measure arrays of subresolution apertures as reference materials, establishing new limits of measurement accuracy that approach the atomic scale over a submillimeter field. In a first application of our novel measurement capability, we introduce critical dimension localization microscopy, characterizing our fabrication accuracy and precision, and facilitating tests of nanofabrication processes and quality control of aperture arrays. In a second application, we apply these stable reference materials to answer open questions about the apparent instability of fluorescent nanoparticles that commonly serve as fiducial markers. By minimizing and quantifying systematic errors, we enable rigorous confidence in statistical precision as the limit of accuracy for localization microscopy at subnanometer scales.

Keywords: critical dimension; localization accuracy; nanoparticle fiducial; optical microscopy; reference material

INTRODUCTION

Optical microscopy methods of localizing subresolution emitters are broadly useful in such fields as cell biology, nanoscale fabrication, cryogenic physics, and microelectromechanical systems¹. Precision²⁻³ and accuracy are fundamental for all localization measurements⁴⁻⁵. Measurements of single fluorophores often result in localization precision on the order of 10 nm, and subnanometer localization precision is possible⁶ and readily achievable for bright emitters such as subresolution nanoparticles. Whereas improving precision generally requires counting more photons by increasing emission intensity and stability⁷⁻⁸, improving accuracy presents diverse challenges in the calibration of an optical microscope as a nonideal measurement system. This involves not only its discrete parts but also their interactions during a measurement. Such a comprehensive calibration is rarely if ever implemented, causing overconfidence in measurement results with statistical uncertainties at the nanometer scale that are invalid due to larger systematic errors. Such errors can extend into the micrometer scale when localizing emitters over a wide field, as is necessary for imaging microstructures and tracking motion⁹⁻¹⁰. This problem motivates the development of materials, methods, and analyses to improve the accuracy of localization microscopy, as we illustrate in Fig. 1.

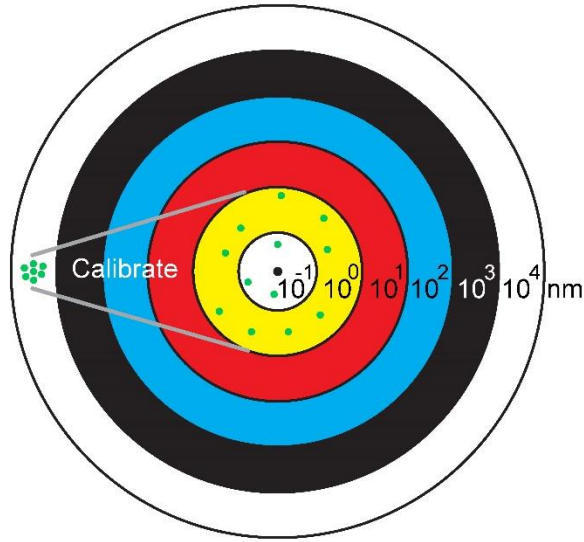


Figure 1. Logarithmic localization target. Green dots are measurement results. Scatter indicates statistical uncertainty from subnanometer localization precision but is not to scale in the outer ring, which indicates systematic errors that can be orders of magnitude larger. Comprehensive calibration enables rigorous confidence in localization precision as the limit of accuracy.

To define the scope of the problem and introduce our solution to it, we briefly review recent developments in related topics. First, test structures are essential to microscope calibration. Whereas random arrays of small particles can suffice for mapping aberrations¹¹⁻¹³, correcting errors due to deviation from nominal magnification requires fabrication of a reference material¹⁴. Arrays of subresolution apertures enable calibration of both aberrations and magnification with uniform sampling of the imaging field¹⁵. Recent studies have used aperture arrays to calibrate the effects of sample orientation and aberrations on three-dimensional localization microscopy¹⁶ and image pixel size¹⁷. However, these studies have not characterized the accuracy and precision of the array pitch, which is critical to magnification calibration and localization accuracy, nor used aperture arrays to evaluate instabilities of microscope systems.

Electron-multiplying charge-coupled-device (EM-CCD) cameras were common at the advent of localization microscopy, and calibration of these cameras is still an active area of research¹⁸. Complementary metal-oxide-semiconductor (CMOS) cameras, with large fields and high sensitivity, but high variability in sensitivity and read noise, are of increasing interest. Initial studies characterized the effects of CMOS noise on localizing single emitters¹⁹ and improved localization of single fluorophores²⁰⁻²¹. However, no study has demonstrated calibration over the full dynamic range of a CMOS camera, which is necessary to maximize signal photons and minimize statistical uncertainty. Previous studies have reported methods for improving illumination uniformity²² and performing flatfield corrections, but have not accounted for all CMOS nonuniformities which can cause localization errors.

Localization analysis extracts subresolution information from optical micrographs. Maximum-likelihood and weighted least-squares algorithms²³⁻²⁴, with specific estimators for CMOS cameras²⁰⁻²¹, compete on the basis of accuracy and efficiency. However, previous studies have not evaluated the performance of each algorithm in the presence of fitting errors, which are common for model approximations of point spread functions which neglect deformations from optical aberrations²⁵⁻²⁷. Another issue is that sensor saturation can occur while imaging bright

emitters over a wide field with nonuniform illumination. Although saturation is typically treated as a fault, it has latent potential for improving localization precision due to the large number of signal photons around the saturation region, but requires tests of localization accuracy.

Finally, in many measurement systems, localization of a fiducial marker, often a subresolution nanoparticle, provides a reference to correct errors from unintentional motion of the sample or the microscope^{7, 28-30}. A typical but critical assumption is that the fiducial is motionless with respect to the sample. However, there are open questions about whether nanoparticle fiducials are truly static on imaging substrates^{11, 23, 28}.

In this study, we address all of these issues through a comprehensive calibration that improves the localization accuracy of a standard optical microscope by up to four orders of magnitude, transforming it into a quantitative metrology system. We calibrate the parts of the system, their interactions during a measurement, and the resulting localization errors. We validate our widefield measurements with scanning measurements and quantify localization errors extending toward the scale of single atomic diameters over a submillimeter field. We apply our new measurement capability to introduce critical dimension localization microscopy of aperture arrays as reference materials and to answer open questions about the apparent motion of nanoparticle fiducials. Our study enables rigorous confidence in statistical precision as the limit of accuracy for localization microscopy at subnanometer scales.

MATERIALS AND METHODS

Aperture arrays

We fabricate square arrays of circular apertures with nominal diameters of 400 nm or 500 nm in bilayer films of titanium and platinum with a total thickness of around 100 nm on silica substrates with a thickness of approximately 170 μm . We use two electron-beam lithography systems to independently pattern arrays and test the accuracy of aperture placement. Both lithography systems are traceable to the SI through laser interferometers that measure stage position with a resolution of approximately 0.6 nm in x and in y to calibrate beam position and to confirm the absence of, or correct for, electron-optical aberrations. To avoid additional errors of aperture placement from stage motion of the lithography systems, we limit the lateral extents of our arrays to single write fields. Further details are in Supplementary Notes 1 and 2, Supplementary Table 1, and Supplementary Figs. 1-4. In the following analysis, we treat each aperture array as a reference material with a mean pitch that is identical to the nominal value of our design, and with random errors in the positions of single apertures due to fabrication precision. After calibrating our measurement system, we quantify aperture position errors.

Nanoparticle fiducials

We test fluorescent nanoparticles as fiducial markers. The manufacturer specifies amorphous polystyrene spheres with a mean diameter of 220 nm, containing boron-dipyrromethene dye molecules with an excitation peak at 505 nm and an emission peak at 515 nm, and with a carboxylic acid coating. We disperse the nanoparticles into pure water at a concentration of 10^6 nanoparticles per μL , deposit 10 μL of the suspension onto a borosilicate coverslip with a thickness of approximately 170 μm and a poly-D-lysine coating, and remove the suspension after 1 min. We expect the nanoparticles to bind electrostatically to the coverslip. We cover the sample surface with pure water and seal it with a silica slide for imaging.

Microscope system

Our optical microscope has an inverted stand, a scanning stage that translates in x and y with a sample holder that rotates around these axes, and a piezoelectric actuator that translates an objective lens in z with a resolution of approximately 10 nm. The objective lens has a nominal magnification of 63 \times and a numerical aperture of 1.2, giving a nominal depth of field of 0.95 μm at the peak illumination wavelength. We reconfigure the microscope to transilluminate aperture arrays or epiilluminate fluorescent nanoparticles with a light emitting diode (LED) array with a peak wavelength of 510 nm and a full width at half maximum of 25 nm. The microscope has a CMOS camera with 2048 pixels by 2048 pixels, each with an on-chip size of 6.5 μm by 6.5 μm . We always operate the camera with water cooling and without on-board correction of pixel noise. We typically operate the camera in fast-scan mode and cool the sensor to -10 $^{\circ}\text{C}$, and calibrate the imaging system for these parameters. In tests of fiducial stability, we operate the camera in slow-scan mode and cool the sensor to -30 $^{\circ}\text{C}$. For fluorescence imaging, we use an excitation filter with a bandwidth from 450 nm to 500 nm, a dichroic mirror with a transition at 505 nm, and an emission filter with a bandwidth from 515 nm to 565 nm. Supplementary Figs. 3-5 show optical micrographs of an aperture array and nanoparticle fiducials.

Sample orientation and position

Optimal use of the aperture array requires control of its orientation around the x and y axes and its z position with respect to the imaging system. First, to minimize errors due to misalignment of the sample relative to the normal of the optical axis³¹, we level the aperture array by iteratively rotating it around its x and y axes, and translating the objective lens through z to simultaneously focus on apertures at the four corners of the imaging field. Supplementary Note 3 describes an alternate method for leveling the sample by analysis of Zernike coefficients, and Supplementary Fig. 6 illustrates our sample holder and presents corresponding results. Then, for all measurements unless we note otherwise, we translate the objective lens through z to obtain a series of images around optimal focus, as Supplementary Note 4 describes and Supplementary Fig. 7 shows. We image at array centers or note otherwise.

Camera calibration

For each pixel i , we measure pixel value offset o_i and read noise $\sigma_{i,read}^2$ as the mean and variance, respectively, of 60000 images²⁰ with the camera shutter closed. We determine flatfield correction factors by imaging a white, planar object that is far from optimal focus and effectively featureless, at nine illumination levels spanning the dynamic range of the imaging sensor,

$F_i = \frac{\bar{I}_i - o_i}{\bar{I}}$, where \bar{I}_i is the mean value of pixel i from 15000 images at an illumination level, o_i is the pixel value offset, and \bar{I} is the mean value of \bar{I}_i from all pixels. The total noise of each pixel is the variance of the pixel value minus the pixel value offset from the 15000 images at an illumination level. Supplementary Fig. 8 shows plots and histograms of pixel value offset and read noise.

Curve fitting

We fit models to data using the method of damped least squares or we note otherwise.

RESULTS AND DISCUSSION

Aperture array

Transillumination of the apertures at wavelengths of around 510 nm produces an array of point sources, as Fig. 2 and Supplementary Fig. 3 show. An array pitch of at least 5 μm ensures that the point spread functions of adjacent apertures do not overlap significantly, as Supplementary Fig. 4 shows.

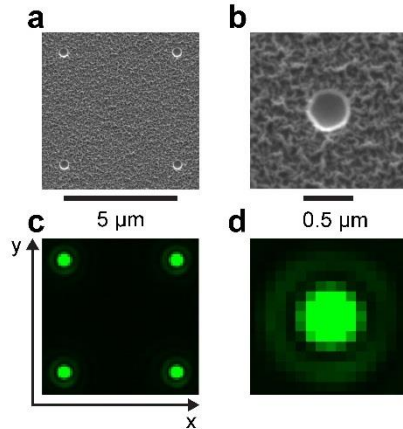


Figure 2. Aperture array. (a-b) Scanning electron micrographs showing representative apertures in a bilayer of titanium and platinum on a silica substrate. (a) The array has a nominal pitch of 5 μm . (b) Each aperture has a nominal diameter of 400 nm and a smaller functional diameter due to nonvertical sidewalls. (c-d) Brightfield optical micrographs showing representative apertures transmitting light. False color represents the illumination wavelengths of around 510 nm. (c) Four apertures form unit cells for pitch analysis. (d) The image of a single aperture approximates the point spread function of the imaging system.

CMOS localization

Accurate localization of aperture images requires calibration of our CMOS camera, including measurements of the total noise of individual pixels, calculation of flatfield corrections, and the dependence of these characteristics on pixel value over the full dynamic range of the imaging sensor, as Fig. 3 shows. The total noise, or variance, of each pixel value includes contributions from read noise, shot noise, and fixed-pattern noise. The flatfield correction removes variation in pixel value due to pixel gain, illumination nonuniformity, and sensor packaging.

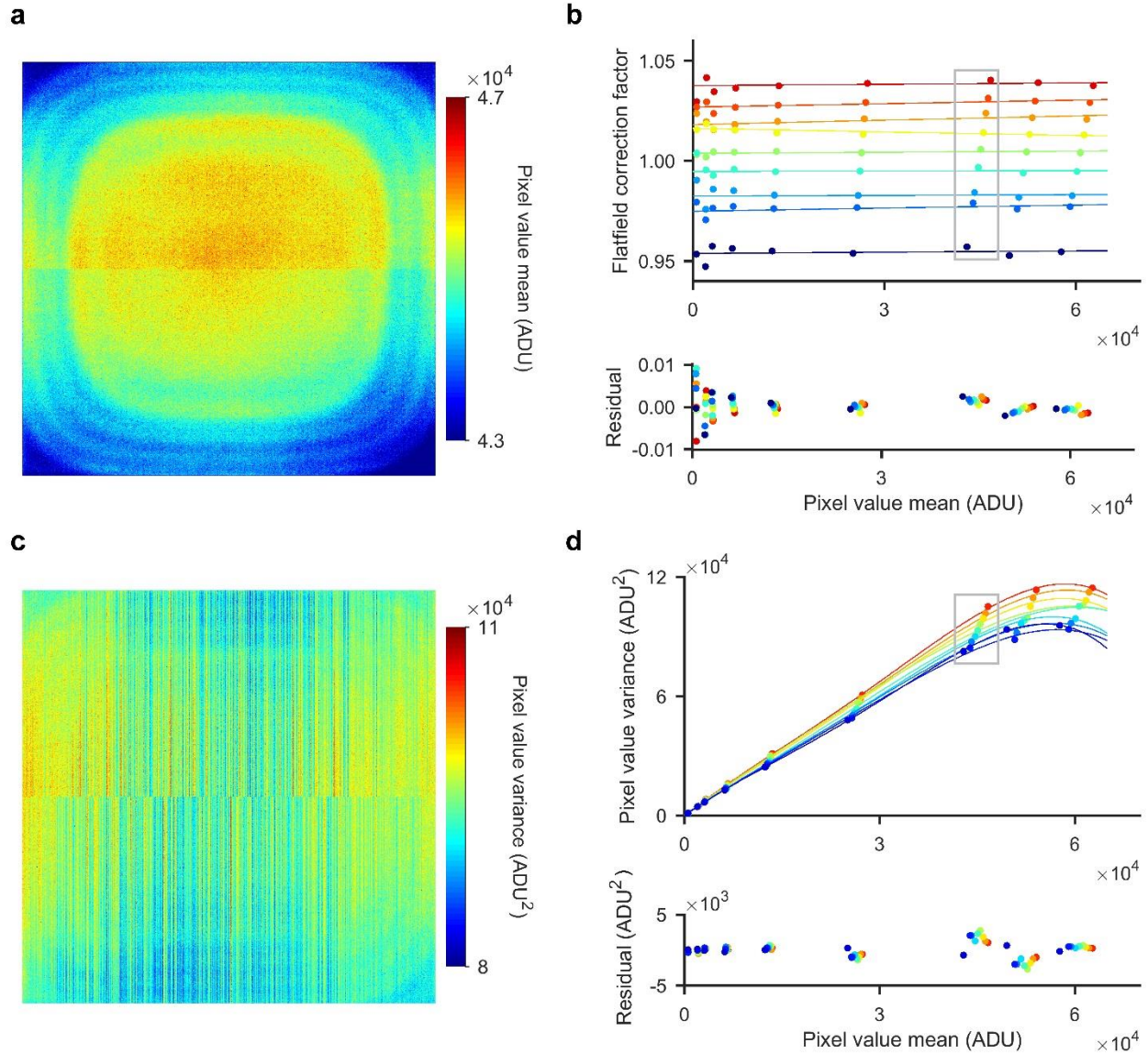


Figure 3. CMOS camera. (a) Plot showing pixel value mean in analog-to-digital units (ADU) from the average of 15000 images at one of nine illumination levels. Nonuniformity results from the illumination profile, sensor packaging, and CMOS architecture. (b) Plot showing flatfield correction factors for nine representative pixels as a function of pixel value mean. The gray box encloses data from the illumination level in (a). The factors abruptly increase at low values and then remain nearly constant for the remaining 95 % of the dynamic range. A linear function empirically approximates the factors over the full dynamic range. (c) Plot showing pixel value variance corresponding to the pixel value mean in (a). Nonuniformity results from sensor packaging and amplifier columns. (d) Plot showing pixel value variance, including contributions from shot noise, read noise, and fixed-pattern noise, as a function of pixel value mean for nine representative pixels. The gray box encloses data from the illumination level in (a, c). A quartic polynomial empirically approximates the pixel value variance over the full dynamic range.

Sensor packaging causes significant variation in pixel value across the field, motivating a flatfield correction, as per Ref. 21 but not Ref. 20. This correction increases abruptly with pixel value mean through the bottom 5 % of the dynamic range and then remains nearly constant over the remaining 95 %, as Fig. 3a-b shows. A recent study did not identify this trend but presented localization algorithms that still achieved the Cramér–Rao lower bound²¹. Therefore, we use the constant correction in our analysis of bright emitters, with pixel values that span the full dynamic range. However, the abrupt increase at low pixel values may be more important for dim emitters. We also find that pixel value variance does not depend linearly on pixel value mean over the full dynamic range, as Fig. 3c-d shows. This contrasts with linear approximations from Poisson statistics at low pixel values. A quartic polynomial is a better approximation, but in a comparison to Refs. 20-21, we find that the linear approximation results in localization that is both sufficiently accurate and computationally efficient. Further details are in Supplementary Note 5 and Supplementary Table 2. These results show that CMOS cameras are even more nonuniform than previous studies have reported, with subtle effects on localization accuracy.

Fitting errors

Previous studies have not fully explored the effects of fitting errors^{24, 32} on the performance of either maximum-likelihood²⁰ or weighted least-squares²¹ estimation. There are arguments for and against both algorithms^{21, 23}. Rather than strictly adhering to one or the other, we evaluate the performance of both for localizing isotropic emitters with systematic underestimation or overestimation of regions of the point spread function. Figure 4 shows a bivariate Gaussian approximation of an experimental point spread function,

$$G_{biv} = A \cdot \exp - \left(\frac{1}{2(1-\rho^2)} \left[\frac{x^2}{\sigma_x^2} - 2\rho \frac{xy}{\sigma_x\sigma_y} + \frac{y^2}{\sigma_y^2} \right] \right) + C, \quad (\text{Eq. 1})$$

where A is the amplitude, x is the position of the peak in the x direction, y is the position of the peak in the y direction, σ_x is the standard deviation in the x direction, σ_y is the standard deviation in the y direction, ρ is the correlation coefficient between the x and y directions, and C is a constant background. This is an extension of the common univariate Gaussian approximation, with some empirical ability to model asymmetry from optical aberrations^{15, 33}. Such asymmetry can be significant, as Fig. 4 shows for the corner of the field, 140 μm away from its center.

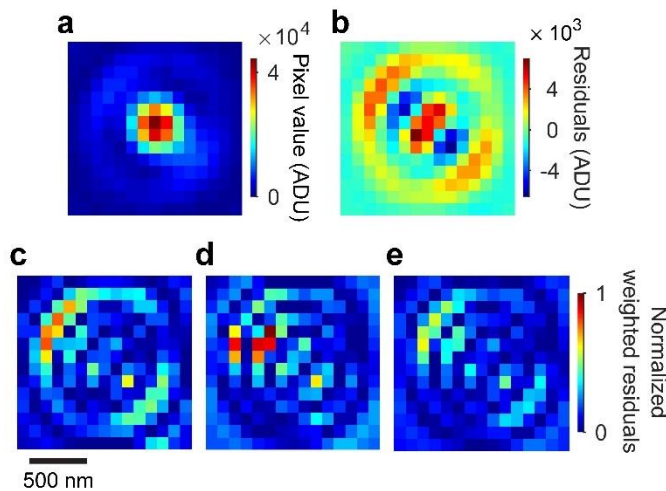


Figure 4. Fitting errors. (a) Optical micrograph showing a point spread function with asymmetry from aberrations. We fit a bivariate Gaussian model to the image to study model overestimation

or underestimation of data for different algorithms. **(b)** Plot showing the residuals from an optimal fit. **(c-e)** Plots showing the squared and weighted residuals on a normalized scale from (c) weighted least-squares estimation, (d) maximum-likelihood estimation, and (e) a hybrid objective function. (c) shows inappropriate weighting of regions of the first Airy ring, while (d) shows inappropriate weighting of regions between the Airy ring and central peak. (e) shows more uniform weighting than either (c) or (d).

We introduce a hybrid objective function as a general solution to this problem of algorithm selection, reducing the impact of fitting errors regardless of whether the model systematically overestimates or underestimates the data,

$$\hat{\Theta} = \operatorname{argmin} \left[\sum \frac{(I-E)^2}{\max(I,E) + \sigma_{read}^2} \right], \quad (\text{Eq. 2})$$

where $\hat{\Theta}$ is the estimate for the parameter set $\hat{\Theta} = \{A, \sigma_x, \sigma_y, \rho, x, y, C\}$, I is the experimental pixel value, E is the expected or model pixel value, and σ_{read}^2 is the read noise. The use of $\max(I,E)$ selects between weighted least-squares ($I > E$) or maximum likelihood ($I < E$) to reduce inappropriately large weights for pixels with significant fitting errors. Further details are in Supplementary Note 6. Clearly, eliminating fitting errors would be ideal. However, most localization algorithms do not account for variable deformation of the point spread function due to optical aberrations – one requires their absence³⁴ – making the above analysis necessary for maximizing their performance. We subsequently quantify localization error, which includes any effects of fitting errors.

Pixel saturation

As the amplitude of a point spread function exceeds the dynamic range of the imaging sensor, pixel values saturate. Although saturation is commonly treated as a defect, we find that the large number of signal photons around the saturation region can actually improve localization precision, at the cost of a tolerable degradation of localization accuracy. We simulate univariate Gaussian approximations of point spread functions with amplitudes that approach and exceed saturation of a 16-bit imaging sensor, as Supplementary Fig. 9 shows. We modify our localization algorithm to include our knowledge of saturation, finding that localization accuracy and precision are independent of this modification. Supplementary Note 7 provides details of this modification, and Supplementary Table 3 shows localization results. In addition, localization is robust to weighting the residuals of the fit to either include or ignore saturated pixels. These surprising results enable not only quantitative analysis but also practical advantage of a signal photon count which results in pixel value saturation.

Aberration effects

To calibrate the effects of optical aberrations on localization accuracy, we scan the aperture array through focus for three-dimensional characterization of the point spread function, enabling analysis of field curvature, point spread function asymmetry, and distortion due to variation of magnification over the field. We locate optimal focus at each aperture position across the field as the z position that maximizes the amplitude of each point spread function, as Supplementary Fig. 7 shows. The field curves over a range in z of nearly 500 nm, as Fig. 5a,b show. We confirm the effective flatness of the aperture array, as Supplementary Fig. 2 shows. The complex curvature of the field, in particular near its center and corners, strongly motivates the use of an aperture array to uniformly sample the field. Such field curvature has several important consequences.

First, not all objects across the field can be at optimal focus simultaneously. For stable emitters and time permitting, field curvature motivates scanning through z to acquire multiple images that completely sample optimal focus across the field, whereas acquisition of a single image requires a compromise focal position, which we define as $z = 0$ in Fig. 5b. This degrades the accuracy of localization measurements due to defocus of some point spread functions, as follows.

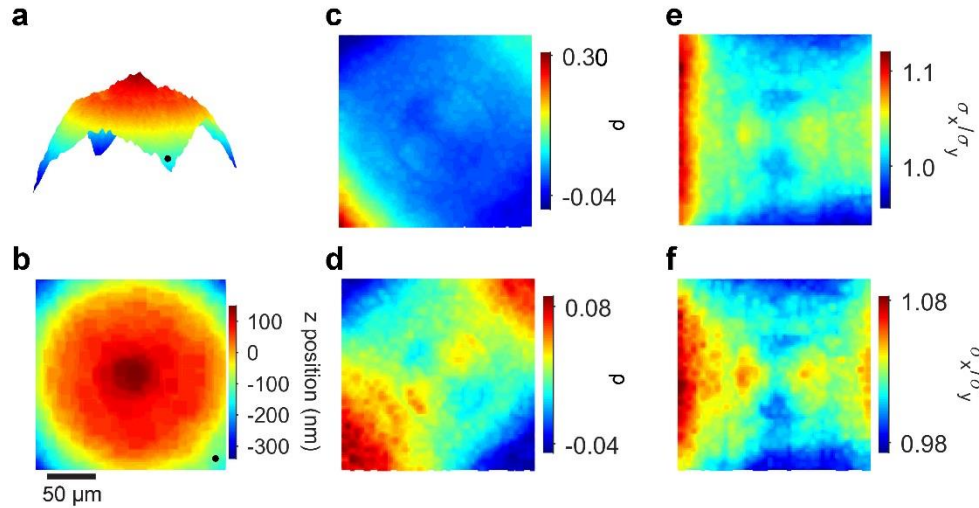


Figure 5. Field curvature and point spread function asymmetry. **(a, b)** Plots showing the curving field of the imaging system. The black dots mark the same corner. Optimal focus for a single image is at $z = 0$ nm. **(c)** Plot showing a larger range of ρ from a single image at optimal focus, maximizing the mean amplitude of 1 600 point spread functions. **(d)** Plot showing a smaller range of ρ from multiple images along the curving field, maximizing the amplitude of each point spread function. **(e)** Plot showing the ratio σ_x/σ_y from a single image at optimal focus. **(f)** Plot showing the ratio σ_x/σ_y from multiple images along the curving field. For these plots and subsequent plots of optical properties, we show linear interpolations of data between apertures.

Aberrations cause asymmetries of the point spread function³⁵, which we characterize by the dimensionless parameters ρ and the ratio σ_x/σ_y . Imaging through focus allows characterization of aberration effects in two ways, as Fig. 5 shows. First, we measure these dimensional parameters within one image at the z position which maximizes the mean amplitude of the point spread functions, but at which only some apertures are in optimal focus, as Fig. 5c,e show. This is consistent with many methods of image acquisition. Next, we measure these dimensionless parameters through focus over the curving field at which all apertures are in optimal focus, as Fig. 5d,f show, reducing the range of ρ by a factor of approximately three but having little effect on σ_x/σ_y . This approach is appropriate for quasistatic imaging through focus of stable emitters. Either analysis can improve localization of dim emitters by fixing values of model parameters of the point spread function or providing accurate initial guesses in minimization algorithms, which can be important for localization accuracy.²⁴

We correct position errors from aberration effects. From one micrograph which maximizes the mean amplitude of point spread functions across the imaging field, we localize each aperture and perform a similarity transformation to map the resulting positions to an ideal array with a pitch of 5 μm, corresponding to our design. In this transformation, planar translation and rotation align the arrays, and uniform scaling determines the mean value of image pixel size. The

differences between the positions that we measure and the corresponding positions in the ideal array define position errors, including statistical uncertainties and systematic errors from measurements, and position errors from fabrication precision. The transformation scale factor gives a mean value of image pixel size of 99.94 nm, which is 3 % smaller than the nominal value of 103 nm. Using the nominal value of image pixel size results in gross measurement errors greater than $4.5 \mu\text{m}$, as Fig. 6a-c shows. Using the mean value of image pixel size from the similarity transformation reduces measurement errors by a factor of more than 18, however, they are still as large as 250 nm, as Fig. 6d-f shows. These measurement errors are due primarily to pincushion distortion, but also to field curvature and deformation of the point spread function. This level of accuracy is comparable to previous studies of magnification calibration that average over these effects in determining a mean value of image pixel size¹⁴, clearly demonstrating the necessity of sampling the field to further reduce systematic errors.

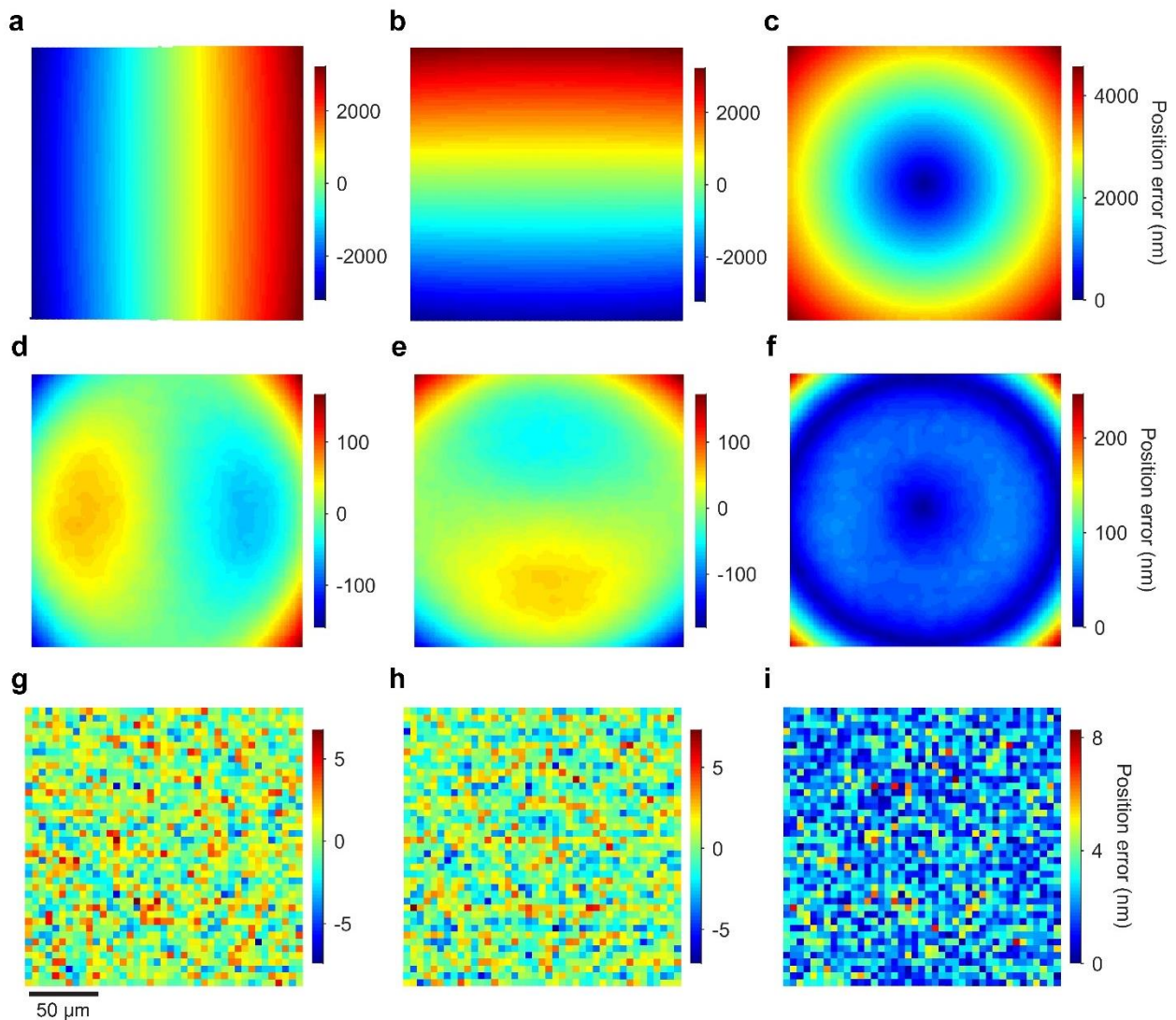


Figure 6. Position errors. (a-c) Plots showing position errors due mostly to measurement errors from using the nominal value of image pixel size of 103 nm in (a) the x direction, (b) the y direction, and (c) total magnitude. (d-f) Plots showing position errors due mostly to measurement errors from using a uniform value of image pixel size of 99.94 nm in (d) the x direction, (e) the y

direction, and (f) total magnitude. **(g-i)** Plots showing position errors due mostly to fabrication precision of the aperture array in (g) the x direction, (h) the y direction, and (i) total magnitude, after applying a correction model to (d-f). Data markers correspond to single apertures.

Error correction

We model these measurement errors by fitting them with the first 73 Zernike polynomials³⁶, giving a correction for any field position. We do not use Zernike polynomials of higher order, as they have spatial frequencies comparable to the array pitch, and result in obviously incorrect model parameters that capture position errors from fabrication precision. We further investigate this effect by simulation, finding a systematic error of less than 0.05 nm for our aperture arrays and providing insight for future optimization, as Supplementary Fig. 10 shows. The correction reduces errors by another factor of 30, resulting in position errors in x and y that are apparently random, as Fig. 6g-i shows. Mean errors are zero by definition of the similarity transformation and Table 1 shows standard deviations for this standard array. We revisit these quantities below to clarify their meaning.

Even though the nominal depth of field of nearly 1 μm greatly exceeds the z-position resolution of 10 nm, position errors in x and y are sensitive to changes in z as small as 10 nm, showing a radial deformation of the field with measurable effects on subnanometer localization, as Supplementary Fig. 11 shows. For z positions beyond 150 nm from optimal focus, the standard deviation of position errors increases by over 1 nm, as Supplementary Fig. 11 shows. This sensitivity indicates the importance of the z-position stability of the microscope system, as we investigate below.

As an example of applying the error correction to experimental data, we translate the standard aperture array in x and y and measure a region that is different from the central region that we use to develop the correction model, giving a subnanometer increase in the standard deviation of position errors that is consistent with variation in z position, as Table 1 and Supplementary Fig. 12 show.

Table 1. Standard deviation of aperture position errors from widefield measurements

Array	x direction (nm)	y direction (nm)
Standard, central region	1.95 ± 0.03	1.97 ± 0.03
Standard, different region	2.46 ± 0.04	2.40 ± 0.04
Low current, long dwell	2.43 ± 0.04	2.00 ± 0.03
Low current, many passes	2.11 ± 0.04	1.35 ± 0.02

Uncertainties are one standard error of the standard deviation³⁷

Critical dimension localization microscopy

We have assumed the absence of systematic effects of electron-optical aberrations on fabrication accuracy, which would corrupt calibration of the systematic effects of photon-optical aberrations. We test this assumption in two ways. First, since the lateral extent of the aperture array exceeds that of the imaging field, we can independently measure different regions of the array. If the effects of electron-optical aberrations were significant, then the correction would include their effects at the array center, resulting in systematic errors upon correction of other regions. We find no such errors, as Supplementary Fig. 12 shows. Second, we laterally scan 100 pairs of apertures, as Fig. 3a shows, through the central 1 % of the imaging field area, sampling the full extent of the aperture array. These measurements are nearly free from aberration effects

due to the high uniformity of this small area, as Figs. 5 and 6d-f show. As well, pitch values within unit cells of the array are independent of the resolution and repeatability of the scanning stage of the microscope system. We find no systematic variation in pitch, as Supplementary Fig. 13 shows, further indicating the absence of appreciable systematic effects from electron-optical aberrations.

To validate our widefield measurements of position errors, we scan and image all apertures in Fig. 6 through the center 1 % of the field area. For 1 600 pairs of apertures, these scanning measurements give consistent results, but only superficially. Supplementary Table 4 shows the pitch variance for each measurement. A deeper analysis of scanning and widefield measurements shows that each includes multiple sources of error and enables discrimination between them. Supplementary Note 8 provides further details. From this analysis, we determine a standard deviation of position errors due to fabrication precision of $1.71 \text{ nm} \pm 0.05 \text{ nm}$ in x and $1.81 \text{ nm} \pm 0.05 \text{ nm}$ in y,³⁸ as well as a widefield localization error that ranges from $0.11 \text{ nm} \pm 0.07 \text{ nm}$ ³⁸ for a systematic error to $0.72 \text{ nm} \pm 0.19 \text{ nm}$ ³⁸ for a random error, independent of localization precision. These uncertainties are standard deviations. Virtually all measurements have errors that limit accuracy at some scale. Our quantification of such errors, including any effects of errors from fitting point spread functions and capture of position errors from fabrication precision by the correction model, is an important advance for localization microscopy. One metric to assess our measurements is the ratio of field size to localization error of at least 2.8×10^5 and at most 1.5×10^6 . To our knowledge, this is the most accurate localization measurement in widefield optical microscopy ever.

In a novel test of fabrication accuracy, we pattern an independent aperture array using a second lithography system that is also traceable to the SI with subnanometer error. Widefield measurements show that the two arrays differ in mean pitch by 0.01 pixels or approximately 1 nm. Assuming that any systematic errors of these measurements are equal, then the difference in mean pitch is very statistically significant with a p-value of 0.0006, but exceeds the position resolution of the lithography stages by less than a factor of two and is approximately half of the standard deviation of position errors due to fabrication precision. This provides an estimate of fabrication accuracy, with a relative systematic error of image pixel size of $1 \text{ nm} / 5000 \text{ nm} = 0.02 \%$. Importantly, fabrication accuracy ultimately limits localization accuracy through magnification calibration¹⁷, as Fig. 6a-f shows. However, our analysis of fabrication precision and localization accuracy and precision is $100.00 \% - 0.02 \% = 99.98 \%$ independent of this limitation of the reference material. To our knowledge, this is the most rigorous analysis of a reference material for localization microscopy ever.

Our new measurement capability closes the gap between common optical microscopes and uncommon instruments for critical dimension metrology,³⁹ and is immediately applicable to new tests of aperture arrays. For example, using widefield measurements, we can rapidly quantify the dependence of fabrication precision on process parameters such as dose rate. We decrease the electron-beam current and increase the dwell time by a factor of five with respect to the fabrication process for the standard array. The standard deviation of position errors increases, as Table 1 shows, indicating that fabrication precision degrades with decreasing dose rate. Second, we reduce the dwell time by a factor of eight, and overwrite the pattern eight times. The standard deviation of position errors decreases in the y direction, but systematic errors increase it in the x direction, indicating that fabrication errors compound with pattern overwriting. Table 1 shows these values and Supplementary Fig. 14 shows further details of these results, which are all roughly consistent with the manufacturer specification of beam positioning of 2 nm, but require

critical dimension metrology to elucidate. The high speed and low cost of optical microscopy would facilitate quality control in a manufacturing process of aperture arrays as reference materials.

Nanoparticle fiducials

Transillumination of the aperture array produces point sources that are static with respect to the imaging substrate at any scale that is relevant to our measurements, providing a stable reference material to evaluate any apparent motion of fluorescent nanoparticles as fiducial markers. We localize apertures or nanoparticles in an image series and quantify the apparent relative motion of each point source as the root-mean-square error of a two-dimensional rigid transform between the point clouds from a pair of images. For pairs of consecutive images, this apparent motion defines the measurement uncertainty. Further details are in Supplementary Note 9. This eliminates unintentional motion of the measurement system in x and y , but not in z , as a source of error. For a static array of point sources, the root-mean-square errors have a normal distribution with a standard deviation due to localization uncertainty, primarily from shot noise and background noise. The Cramér–Rao lower bound allows assessment of such statistical uncertainty, whereas the aperture array allows assessment of apparent motion due to other sources of measurement uncertainty. In this evaluation, the time that is necessary for our microscope to image through focus provides a natural boundary between faster and slower time scales.

First, we analyze rigid transforms of consecutive images of the aperture array to test for motion at a time scale of 10^{-1} s. Apertures show apparent translation in a single lateral dimension with standard deviations ranging from 0.30 nm to 0.65 nm, or a factor of 1.2 to 2.0 times the Cramér–Rao lower bound for each aperture, as Supplementary Fig. 15 shows. We analyze fluorescent nanoparticles on a microscope coverslip, finding that the same metric ranges from 0.30 nm to 0.85 nm, or a factor of 1.2 to 1.9 times the Cramér–Rao lower bound for each nanoparticle, as Supplementary Fig. 15 shows. This demonstrates that the nanoparticles do not move in any way that we can measure at these scales.

Next, we analyze rigid transforms of each image with respect to the first image to extend the time scale to 10^1 s. We observe apparent motion of apertures in the radial direction and with displacements that increase with distance from the field center, as Fig. 7 shows. For comparison, Supplementary Fig. 16 shows apparent motion that is qualitatively similar from imaging through focus. We conclude that this apparent motion is consistent with unintentional motion of the measurement system in z , increasing errors of the rigid transform.

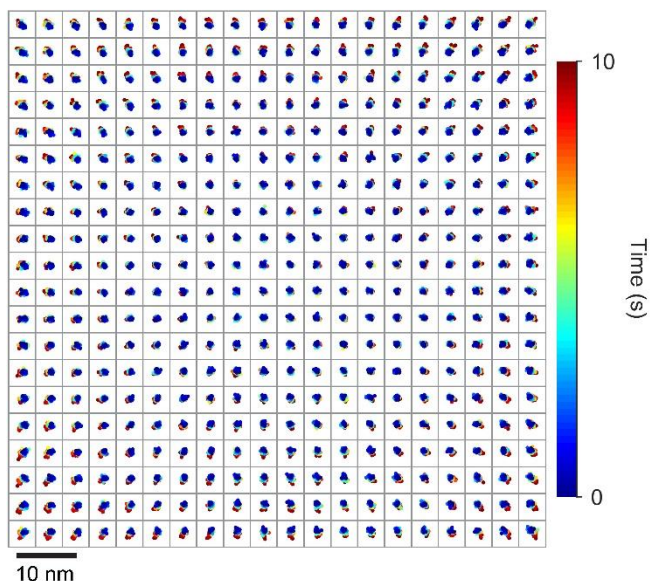


Figure 7. Apparent motion. Grid of scatterplots, each corresponding to a single aperture, showing apparent motion in the radial direction due to unintentional motion of the measurement system in z over 10^1 s. The grid spacing indicates an aperture array pitch of $10\ \mu\text{m}$. The scale bar corresponds to the scatterplots.

At slower time scales, we can image through focus to decrease unintentional motion in z to less than our positioning resolution of $10\ \text{nm}$, finding the z position that minimizes the error of the rigid transform, as Supplementary Fig. 7 shows. This complements other physical²⁸ and analytical³³ methods to mitigate focus instability. Over 10^4 s, both apertures and nanoparticles exhibit similar apparent motion within their respective mean uncertainties of approximately $0.43\ \text{nm}$ for apertures and $0.55\ \text{nm}$ for nanoparticles, as Supplementary Fig. 17 shows, probably due to differences in z position below our position resolution between images. Considering that the apertures are static, we conclude that the nanoparticles are static.

We can now answer open questions about the apparent motion of fluorescent nanoparticles on imaging substrates, and provide a method to evaluate the stability of any particular experimental system. We find that, for a common experimental implementation, fluorescent nanoparticles can function as truly motionless fiducials at subnanometer scales. Previous studies reporting nanoparticle motion have not fully characterized the interactions of the components of the measurement system, in particular unintentional motion along the optical axis, using a stable reference material such as the aperture array. It is evident from our study that this source of motion of any fiducial is most clear over a wide field and upon comparison to other fiducials in an array, and is less apparent over a smaller field or at the field center.

CONCLUSIONS

It is remarkable that the optical microscope, which has for centuries enabled observations at the micrometer scale, can potentially achieve localization uncertainty at the atomic scale over a millimeter field. Whereas the precision of such measurements is largely a function of emitter intensity and stability, the accuracy depends on a comprehensive calibration of the parts of a measurement system and their interaction. This is rarely if ever implemented, causing overconfidence in measurement results with small statistical errors but large systematic errors.

Such false precision is becoming increasingly problematic as measurements more frequently achieve nanoscale localization precision, and as imaging fields extend into the milliscale and multifocal⁴⁰ and spectroscopic⁴¹ methods emerge to exploit wide fields. In this article, we have revealed the surprising extent of this widespread problem and presented a practical solution to it.

By combining widefield and scanning measurements, we have calibrated our microscope system through error correction and characterized our aperture arrays through error analysis. Our subnanometer localization error over a submillimeter field enables two applications. First, critical dimension localization microscopy enables rapid characterization of aperture arrays by widefield imaging, enabling study of nanofabrication processes and quality control of reference materials for microscope calibration. Second, we exploit the stability of aperture arrays to evaluate the stability of nanoparticle fiducials, which multiple studies have called into question. We find that microscope instability can obscure the true stability of fluorescent nanoparticles on an imaging substrate, and we provide a method of evaluating different systems.

In conclusion, by developing powerful and practical approaches to optical microscope calibration, reference material characterization, and particle fiducial evaluation, we have advanced the practice of localization microscopy at subnanometer scales.

ACKNOWLEDGMENTS

The authors acknowledge Glenn Holland for designing and fabricating the stage insert, Kerry Siebein for performing electron microscopy of aperture arrays, and Andras Vladar for reviewing and commenting on the manuscript. The authors acknowledge support of this research under the National Institute of Standards and Technology (NIST) Innovations in Measurement Science Program, the NIST Center for Nanoscale Science and Technology, and the NIST Physical Measurement Laboratory. C. R. C. acknowledges support under the Cooperative Research Agreement between the University of Maryland and the NIST Center for Nanoscale Science and Technology, award number 70ANB10H193, through the University of Maryland.

REFERENCES

1. Mathai, P. P.; Liddle, J. A.; Stavis, S. M., Optical tracking of nanoscale particles in microscale environments. *Applied Physics Reviews* **2016**, *3* (1), 011105.
2. Thompson, R. E.; Larson, D. R.; Webb, W. W., Precise nanometer localization analysis for individual fluorescent probes. *Biophysical Journal* **2002**, *82* (5), 2775-83.
3. McGray, C.; Copeland, C. R.; Stavis, S. M.; Geist, J., Centroid precision and orientation precision of planar localization microscopy. *Journal of Microscopy* **2016**, *263* (3), 227-370.
4. Waters, J. C., Accuracy and precision in quantitative fluorescence microscopy. *The Journal of Cell Biology* **2009**, *185* (7), 1135.
5. Deschout, H.; Zanicchi, F. C.; Mlodzianoski, M.; Diaspro, A.; Bewersdorf, J.; Hess, S. T.; Braeckmans, K., Precisely and accurately localizing single emitters in fluorescence microscopy. *Nature Methods* **2014**, *11* (3), 253-266.
6. Pertsinidis, A.; Zhang, Y.; Chu, S., Subnanometre single-molecule localization, registration and distance measurements. *Nature* **2010**, *466* (7306), 647-51.
7. Colomb, W.; Czerski, J.; Sau, J. D.; Sarkar, S. K., Estimation of microscope drift using fluorescent nanodiamonds as fiducial markers. *Journal of Microscopy* **2017**, *266* (3), 298-306.
8. Yildiz, A.; Forkey, J. N.; McKinney, S. A.; Ha, T.; Goldman, Y. E.; Selvin, P. R., Myosin V Walks Hand-Over-Hand: Single Fluorophore Imaging with 1.5-nm Localization. *Science* **2003**, *300* (5628), 2061.

9. Copeland, C. R.; McGray, C. D.; Geist, J.; Aksyuk, V. A.; Stavis, S. M. Characterization of electrothermal actuation with nanometer and microradian precision, *Solid-State Sensors, Actuators and Microsystems (TRANSDUCERS), 2015 Transducers - 2015 18th International Conference on*, 21-25 June **2015**, 792-795.
10. Copeland, C. R.; McGray, C. D.; Geist, J.; Aksyuk, V. A.; Stavis, S. M., Transfer of motion through a microelectromechanical linkage at nanometer and microradian scales. *Microsystems & Nanoengineering* **2016**, *2* (16055).
11. Mortensen, K. I.; Sung, J.; Flyvbjerg, H.; Spudich, J. A., Optimized measurements of separations and angles between intra-molecular fluorescent markers. *Nature Communications* **2015**, *6* (8621).
12. Hanser, B. M.; Gustafsson, M. G. L.; Agard, D. A.; Sedat, J. W., Phase-retrieved pupil functions in wide-field fluorescence microscopy. *Journal of Microscopy* **2004**, *216* (1), 32-48.
13. Zheng, G.; Ou, X.; Horstmeyer, R.; Yang, C., Characterization of spatially varying aberrations for wide field-of-view microscopy. *Optics Express* **2013**, *21* (13), 15131-15143.
14. Dai, X.; Xie, H.; Li, C.; Wu, Z.; Geng, H., High-accuracy magnification calibration for a microscope based on an improved discrete Fourier transform. *Optical Engineering* **2013**, *52* (11), 114102-114102.
15. T. Matsuzawa, G. R., Y. Eda, T. Morita, Lens evaluation device. *United States Patent* **2010**, US7747101 B2.
16. Diezmann, A. v.; Lee, M. Y.; Lew, M. D.; Moerner, W. E., Correcting field-dependent aberrations with nanoscale accuracy in three-dimensional single-molecule localization microscopy. *Optica* **2015**, *2* (11), 985-993.
17. Copeland, C. R.; McGray, C. D.; Geist, J.; Liddle, J. A.; Ilic, B. R.; Stavis, S. M. Aperure Arrays for Subnanometer Calibration of Optical Microscopes, *International Conference on Optical MEMS and Nanophotonics*, 13-17 August **2017**.
18. Mortensen, K. I.; Flyvbjerg, H., "Calibration-on-the-spot": How to calibrate an EMCCD camera from its images. *Scientific Reports* **2016**, *6*, 28680.
19. Long, F.; Zeng, S.; Huang, Z. L., Localization-based super-resolution microscopy with an sCMOS camera part II: experimental methodology for comparing sCMOS with EMCCD cameras. *Optics Express* **2012**, *20* (16), 17741-59.
20. Huang, F.; Hartwich, T. M. P.; Rivera-Molina, F. E.; Lin, Y.; Duim, W. C.; Long, J. J.; Uchil, P. D.; Myers, J. R.; Baird, M. A.; Mothes, W.; Davidson, M. W.; Toomre, D.; Bewersdorf, J., Video-rate nanoscopy using sCMOS camera-specific single-molecule localization algorithms. *Nature Methods* **2013**, *10* (7), 653-658.
21. Lin, R.; Clowsley, A. H.; Jayasinghe, I. D.; Baddeley, D.; Soeller, C., Algorithmic corrections for localization microscopy with sCMOS cameras - characterisation of a computationally efficient localization approach. *Optics Express* **2017**, *25* (10), 11701-11716.
22. Douglass, K. M.; Sieben, C.; Archetti, A.; Lambert, A.; Manley, S., Super-resolution imaging of multiple cells by optimized flat-field epi-illumination. *Nature Photonics* **2016**, *10* (11), 705-708.
23. Mortensen, K. I.; Churchman, L. S.; Spudich, J. A.; Flyvbjerg, H., Optimized localization analysis for single-molecule tracking and super-resolution microscopy. *Nature Methods* **2010**, *7* (5), 377-81.
24. Abraham, A. V.; Ram, S.; Chao, J.; Ward, E. S.; Ober, R. J., Quantitative study of single molecule location estimation techniques. *Optics Express* **2009**, *17* (26), 23352-23373.

25. Hecht, E., Optics. *Addison Wesley* **1998**, 997, 213-214.
26. Pawley, J.; Masters, B. R., Handbook of biological confocal microscopy. *Optical Engineering* **1996**, 35 (9), 2765-2766.
27. Liu, S.; Kromann, E. B.; Krueger, W. D.; Bewersdorf, J.; Lidke, K. A., Three dimensional single molecule localization using a phase retrieved pupil function. *Optics Express* **2013**, 21 (24), 29462-29487.
28. Carter, A. R.; King, G. M.; Ulrich, T. A.; Halsey, W.; Alchenberger, D.; Perkins, T. T., Stabilization of an optical microscope to 0.1 nm in three dimensions. *Applied Optics* **2007**, 46 (3), 421-427.
29. Grover, G.; Mohrman, W.; Piestun, R., Real-time adaptive drift correction for super-resolution localization microscopy. *Optics Express* **2015**, 23 (18), 23887-23898.
30. Lee, S. H.; Baday, M.; Tjioe, M.; Simonson, P. D.; Zhang, R.; Cai, E.; Selvin, P. R., Using fixed fiduciary markers for stage drift correction. *Optics Express* **2012**, 20 (11), 12177-12183.
31. Arimoto, R.; Murray, J. M., A common aberration with water-immersion objective lenses. *Journal of Microscopy* **2004**, 216 (1), 49-51.
32. Small, A.; Stahlheber, S., Fluorophore localization algorithms for super-resolution microscopy. *Nature Methods* **2014**, 11 (3), 267-279.
33. Ma, H.; Xu, J.; Jin, J.; Huang, Y.; Liu, Y., A Simple Marker-Assisted 3D Nanometer Drift Correction Method for Superresolution Microscopy. *Biophysical Journal* **2017**, 112 (10), 2196-2208.
34. Parthasarathy, R., Rapid, accurate particle tracking by calculation of radial symmetry centers. *Nature Methods* **2012**, 9 (7), 724-726.
35. Blythe, K. L.; Titus, E. J.; Willets, K. A., Objective-Induced Point Spread Function Aberrations and Their Impact on Super-Resolution Microscopy. *Analytical Chemistry* **2015**, 87 (12), 6419-6424.
36. Zernike, v. F., Beugungstheorie des schneidenver-fahrens und seiner verbesserten form, der phasenkontrastmethode. *Physica* **1934**, 1 (7), 689-704.
37. Ahn, S.; Fessler, J. A., Standard errors of mean, variance, and standard deviation estimators. *EECS Department, The University of Michigan* **2003**, 1-2.
38. NIST Uncertainty Machine.
39. Postek, M.; Vadar, A., Critical-Dimension Metrology and the Scanning Electron Microscope: Handbook of Silicon Semiconductor Metrology. *CRC Press* **2001**.
40. Abrahamsson, S.; Chen, J.; Hajj, B.; Stallinga, S.; Katsov, A. Y.; Wisniewski, J.; Mizuguchi, G.; Soule, P.; Mueller, F.; Darzacq, C. D.; Darzacq, X.; Wu, C.; Bargmann, C. I.; Agard, D. A.; Dahan, M.; Gustafsson, M. G. L., Fast multicolor 3D imaging using aberration-corrected multifocus microscopy. *Nature Methods* **2013**, 10 (1), 60-63.
41. Dong, B.; Almassalha, L.; Urban, B. E.; Nguyen, T.-Q.; Khuon, S.; Chew, T.-L.; Backman, V.; Sun, C.; Zhang, H. F., Super-resolution spectroscopic microscopy via photon localization. *Nature Communications* **2016**, 7 (12290).
42. Balram, K. C.; Westly, D. A.; Davanco, M. I.; Grutter, K. E.; Li, Q.; Michels, T.; Ray, C. H.; Kasica, R. J.; Wallin, C. B.; Gilbert, I. J., The nanolithography toolbox. *Journal of Research of the National Institute of Standards and Technology* **2016**, 121.

Supplementary information *for* Subnanometer localization accuracy in widefield optical microscopy

Craig R. Copeland^{1, 2}, Craig D. McGray³, Jon Geist³, Vladimir A. Aksyuk¹, J. Alexander Liddle¹,
B. Robert Ilic¹, and Samuel M. Stavis^{1, *}

¹Center for Nanoscale Science and Technology, National Institute of Standards and Technology, Gaithersburg, Maryland 20899, ²Maryland Nanocenter, University of Maryland, College Park, Maryland 20742, ³Engineering Physics Division, National Institute of Standards and Technology, Gaithersburg, Maryland 20899, *sstavis@nist.gov

INDEX

Supplementary Note 1. Aperture array – fabrication
Supplementary Table 1. Aperture array – specification
Supplementary Note 2. Aperture array – characterization
Supplementary Figure 1. Aperture array – electron microscopy
Supplementary Figure 2. Aperture array – interferometric optical microscopy
Supplementary Figure 3. Aperture array – optical microscopy
Supplementary Figure 4. Aperture array – point spread functions
Supplementary Figure 5. Nanoparticle fiducials
Supplementary Note 3. Sample leveling
Supplementary Figure 6. Sample leveling
Supplementary Note 4. Optimal focus
Supplementary Figure 7. Optimal focus
Supplementary Figure 8. Camera calibration
Supplementary Note 5. CMOS localization
Supplementary Table 2. CMOS localization
Supplementary Note 6. Fitting errors
Supplementary Figure 9. Pixel saturation
Supplementary Note 7. Pixel saturation
Supplementary Table 3. Pixel saturation
Supplementary Figure 10. Fabrication precision and error correction
Supplementary Figure 11. Error is sensitive to focus
Supplementary Figure 12. Error correction across the aperture array
Supplementary Figure 13. Pitch across the aperture array
Supplementary Note 8. scanning and widefield measurements
Supplementary Table 4. Pitch variance
Supplementary Table 5. From pitch variance to position standard deviation
Supplementary Figure 14. Patterning processes
Supplementary Note 9. Rigidity analysis
Supplementary Figure 15. Nanoparticle stability down to 10^{-1} s
Supplementary Figure 16. Apparent motion
Supplementary Figure 17. Nanoparticle stability up to 10^4 s

Supplementary Note 1. Aperture array – fabrication

We fabricate aperture arrays on silica substrates with manufacturer specifications of a thickness of approximately 170 μm , a surface roughness of less than 0.7 nm root-mean-square, a scratch number of 20, a dig number of 10, a flatness deviation of $2.5 \times 10^{-4} \text{ nm}\cdot\text{nm}^{-1}$ to $5.0 \times 10^{-4} \text{ nm}\cdot\text{nm}^{-1}$, and a parallelism of less than 0.15 mrad. We deposit a titanium film with a thickness of approximately 10 nm as an adhesion layer, a platinum film with a thickness of approximately 80 nm for optical opacity, a positive-tone electron-beam resist film with a thickness of approximately 120 nm, and an aluminum film with a thickness of approximately 15 nm for charge dissipation.

We pattern aperture arrays using two electron-beam lithography systems, enabling comparison of independent reference materials to test fabrication accuracy, and fabrication of different types of aperture arrays that use and test the different operating modes of the systems. Other than different load locks, the lithography systems have nearly identical hardware. Each system has a scanning stage with two laser interferometers to measure stage position in x and in y. The resolution of a stage position measurement is $632.8 \text{ nm} / 1024 = 0.6180 \text{ nm}$, with traceability to the SI through the operating wavelength of the helium–neon laser. One lithography system operates four of five electron-optical lenses and has a write field of 1 mm by 1 mm, which is useful to avoid stitching errors in patterning aperture arrays for widefield imaging, and has a specification for beam placement of 2 nm. The electron-beam current for this system is typically 1.0 nA, although we reduce it in some tests of patterning parameters that we note. The other lithography system operates five of five electron-optical lenses and has a better specification for beam placement of 0.125 nm, which nominally improves fabrication precision, which we test, but does so over a smaller write field of 62.5 μm by 62.5 μm . The electron-beam current for this system is 1 nA. We perform a Monte Carlo simulation of electron trajectories in the film stack to correct the pattern data for proximity effects at an accelerating voltage of 100 kV, and we fracture the pattern data into polygons.

After electron-beam exposure, we remove the aluminum film with tetramethylammonium hydroxide and cold-develop the electron-beam resist in hexyl acetate. Finally, we mill the apertures with argon ions, using a secondary-ion mass spectrometer to monitor milling products and stop at the top surface of the silica substrate. The electron-beam resist is not trivial to remove after argon-ion milling and does not affect the function of the aperture array in any way that we are aware of, so we leave the electron-beam resist in place.

We design our devices using the Nanolithography Toolbox⁴². Further specifications of aperture arrays are in Supplementary Table 1.

Supplementary Table 1. Aperture array – specification

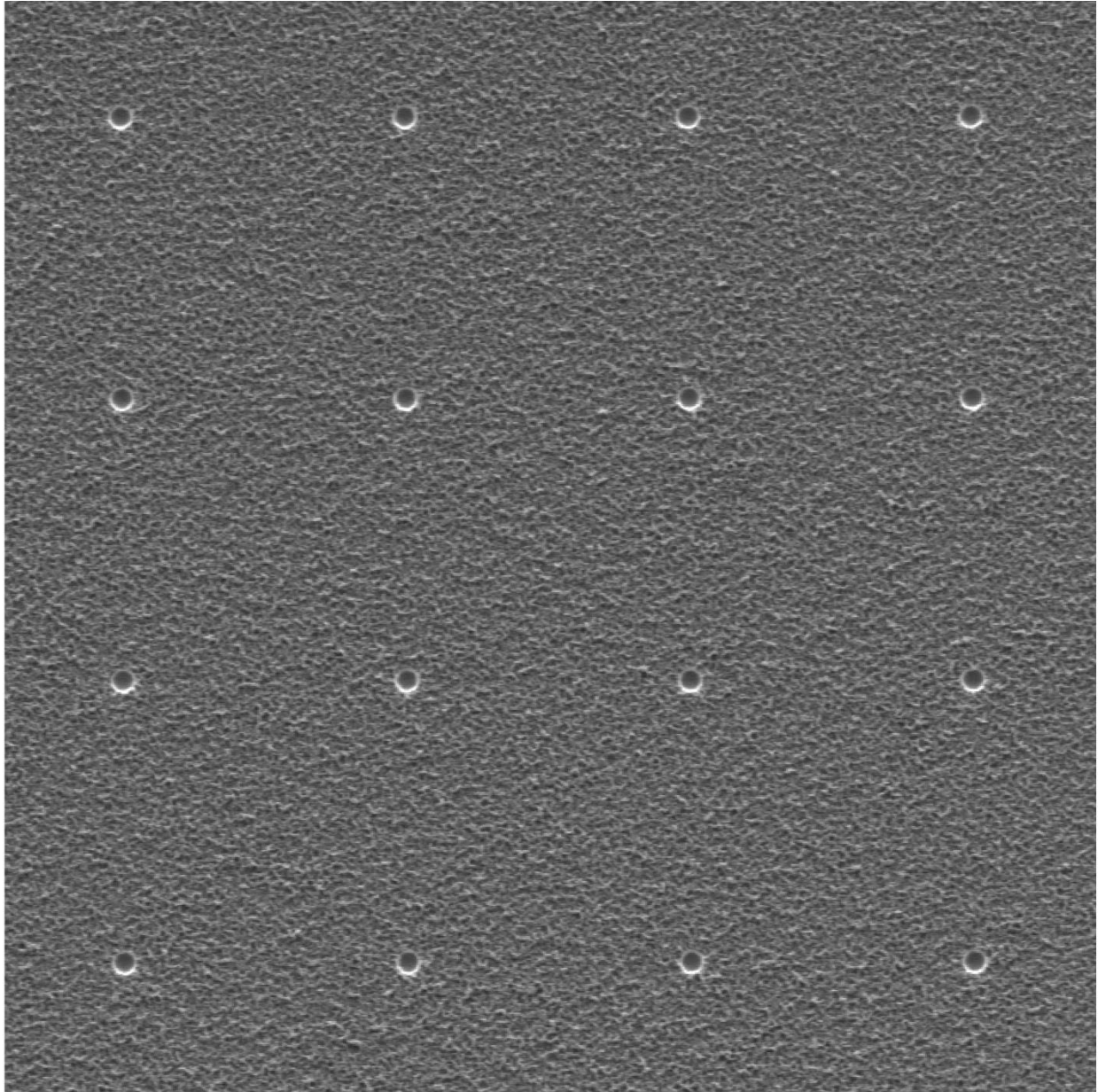
Array pitch (μm)	Array extent (μm)	Nominal aperture diameter (nm)	Platinum thickness (nm)
5, 10	350 \times 350	400	80
5	62.5 \times 62.5	500	80

Supplementary Note 2. Aperture array – characterization

We inspect the aperture array by scanning electron microscopy, as Supplementary Fig. 1 shows. We acquire scanning electron micrographs with an accelerating voltage of 1 kV, using an Everhart-Thornley detector at a working distance of 9 mm. These inspection measurements confirm the presence of approximately circular apertures with shape irregularity at the scale of tens of nanometers and aperture sidewalls that are not vertical, resulting in smaller functional

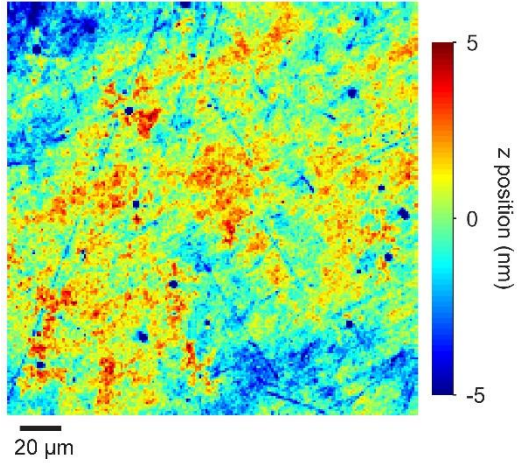
diameters at the silica surface than the nominal diameters at the platinum surface. We do not attempt to quantify array pitch from these electron micrographs. To do so at subnanometer scales would require calibration of the electron microscope and localization analysis that are beyond the scope of this study.

We measure the upper surface topography of the aperture array by interferometric optical microscopy, as Supplementary Fig. 2 shows. This instrument operates at a peak wavelength of 475 nm with a bandwidth of 125 nm. The z position of the piezoelectric stage of this instrument is traceable to the SI through a reference material for step height. We further calibrate this instrument using a reference flat of silicon carbide. We extract the center of the interference pattern as a function of z position as the location of the reflecting surface. We fit the resulting upper surface topography of the aperture array to a plane to level it and analyze the z-position variation of the upper surface as an indicator of the lower interface between silica and titanium. We expect and observe scratches and digs consistent with the polish of the silica substrate transferring through conformal metal films. The standard deviation of z position is 1.76 nm, such that the upper surface is effectively flat within the z-position resolution of 10 nm of our localization microscope. Therefore, in subsequent analysis, we ignore any nonflatness of the aperture array. However, in the production of reference materials for three-dimensional localization microscopy, for example, this issue motivates the specification of even flatter substrates or the analytical correction of any nonplanar surface topography of the aperture array.

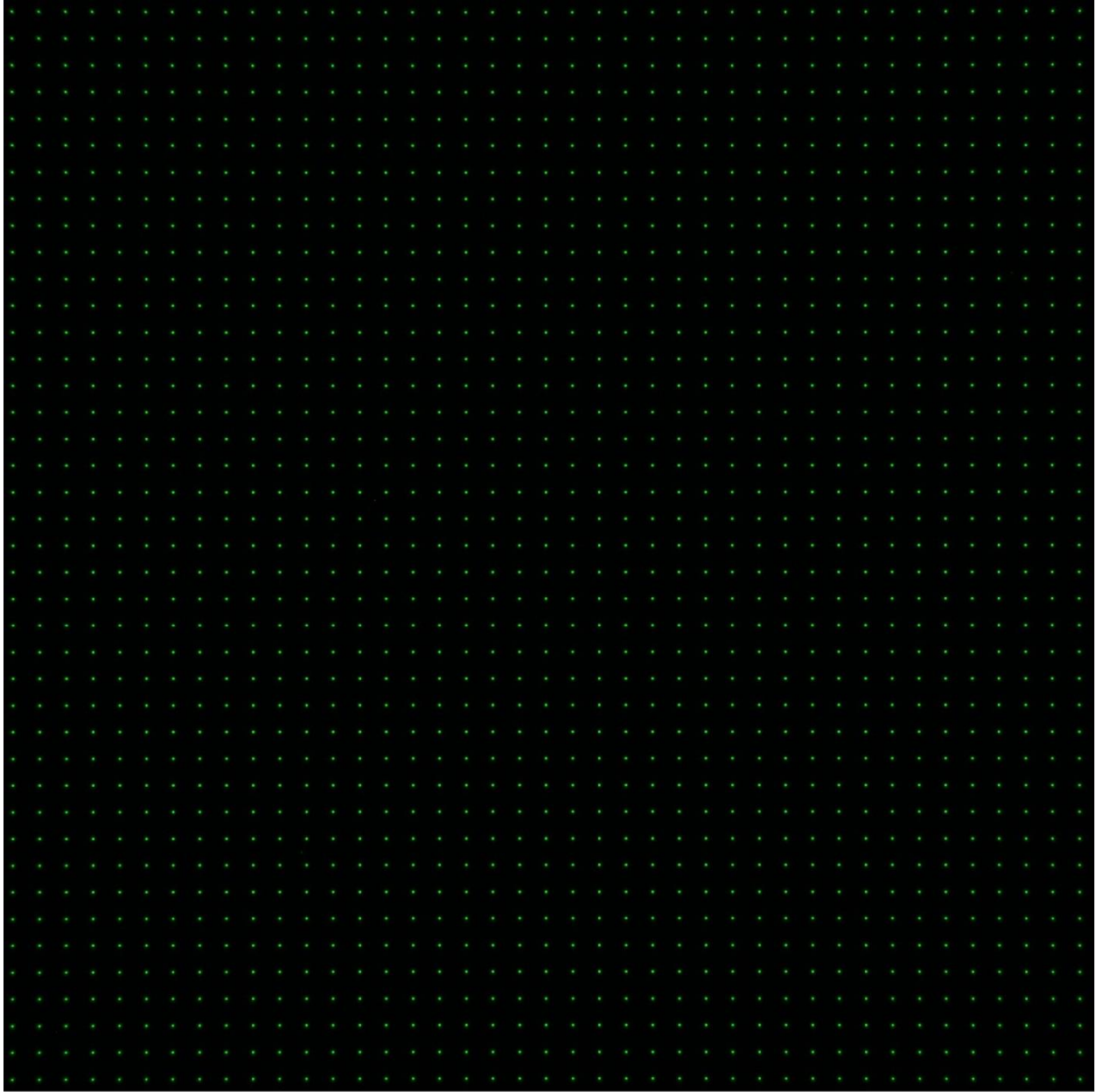


1 μm

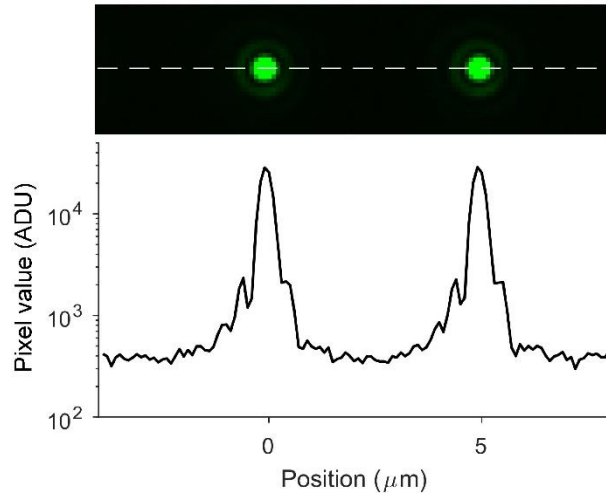
Supplementary Figure 1. Aperture array – electron microscopy. Scanning electron micrograph showing 16 apertures. Surface texture around the apertures is from electron-beam resist.



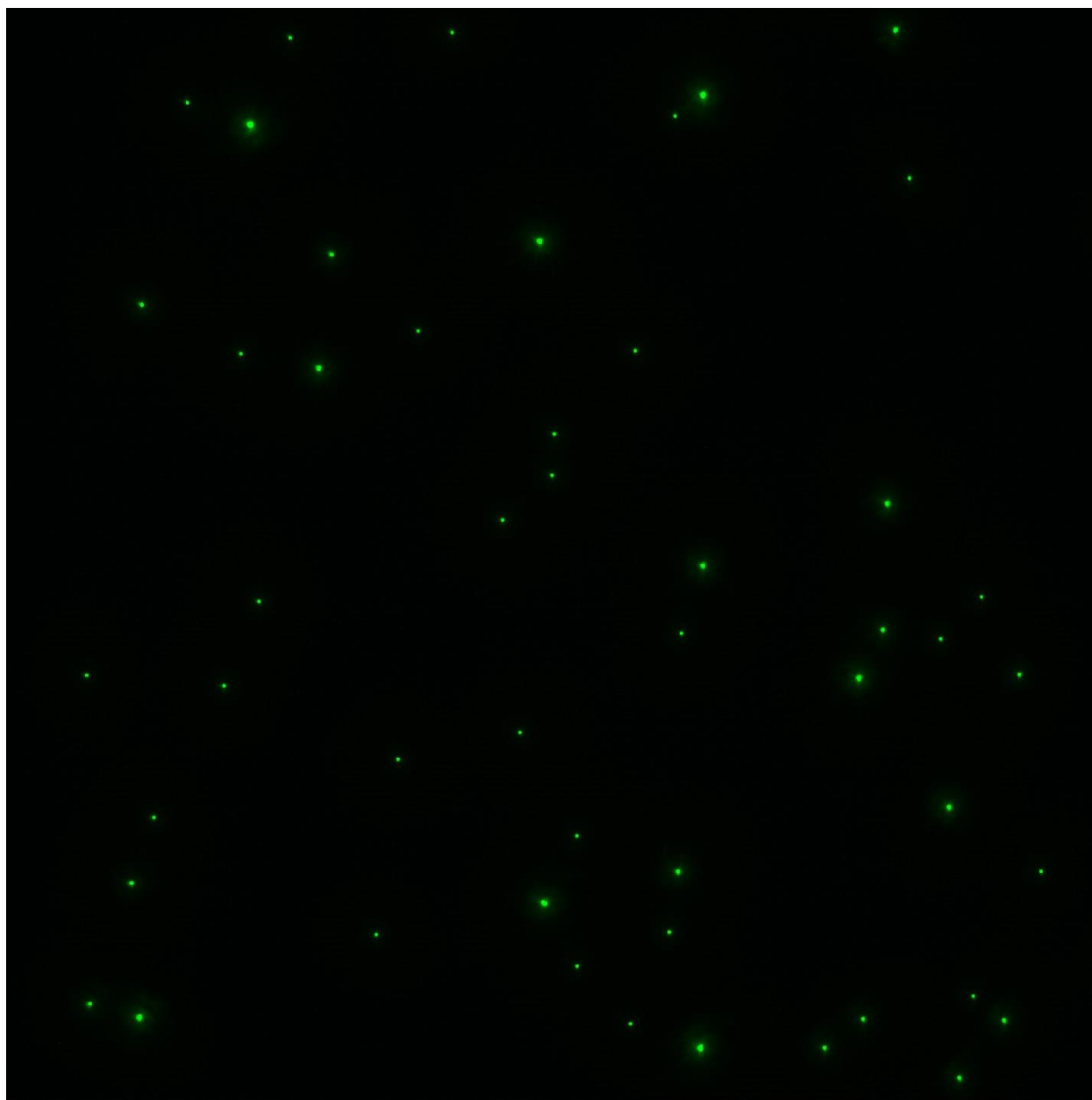
Supplementary Figure 2. Aperture array – interferometric optical microscopy. Interferometric optical micrograph showing the upper surface topography of a representative region corresponding approximately to the aperture array. The apertures are below the resolution of this imaging system. Scratches and digs in the upper surface are consistent with the polish of the lower silica surface. The standard deviation of z position is 1.76 nm.



Supplementary Figure 3. Aperture array – optical microscopy. Brightfield optical micrograph showing the transmission of light through an aperture array over the full field of the imaging system of approximately 200 μm by 200 μm . False color represents the illumination wavelengths of around 510 nm.



Supplementary Figure 4. Aperture array – point spread functions. **(a)** Brightfield optical micrograph showing the point spread functions from two apertures with nominal diameters of 400 nm in an array with a nominal pitch of 5 μm . **(b)** Plot showing pixel value along the white dashed line in (a). The point spread function from the left aperture decays to background by approximately 3 μm from the center position of the aperture. This shows that an array pitch of 5 μm provides sufficient separation of adjacent apertures such that their signals do not appreciably overlap within the region of interest for localization analysis, which is approximately 1 μm around the center position of each aperture. Features resembling Airy rings are clearly evident, indicating subresolution apertures.

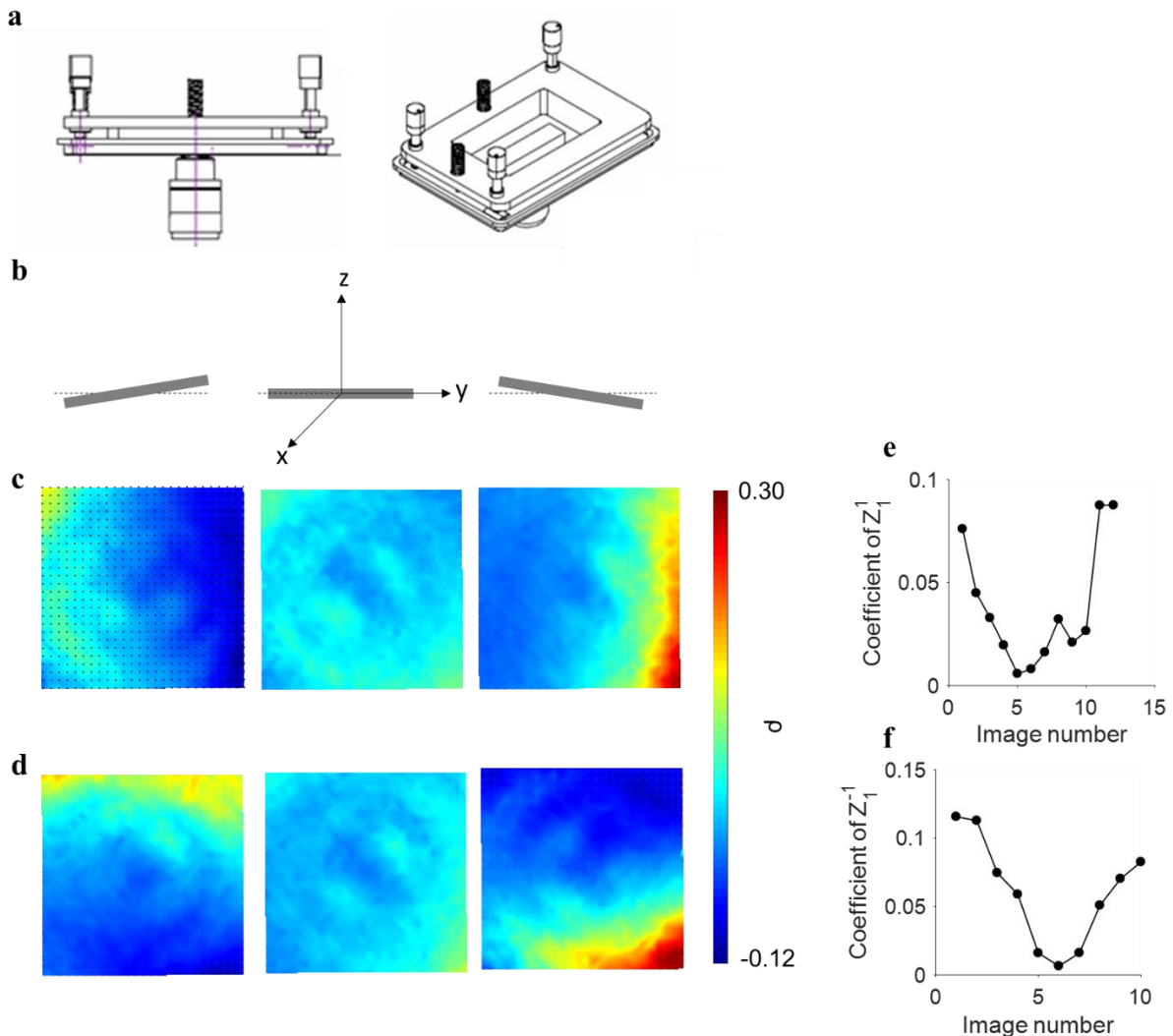


10 μm

Supplementary Figure 5. Nanoparticle fiducials. Fluorescence micrograph showing fluorescent nanoparticles with a carboxylate coating on a borosilicate coverslip with a poly-D-lysine coating. In subsequent analysis, we ignore aggregates of nanoparticles, which are evident as images that are brighter and larger than single point spread functions.

Supplementary Note 3. Sample leveling

We can level a sample with respect to the normal of the optical axis using two different methods. The first exploits piezoelectric actuation and characterization of the z position of the objective lens, as we describe in the main text. The second takes advantage of Zernike theory. Both methods require a stage insert that enables rotation of the sample about the x and y axes, as Supplementary Fig. 6a-b shows. In the second method of leveling a sample, we analyze spatial maps of aberrations of the point spread function across the field. We fit the maps to a linear combination of Zernike polynomials³⁶ in real time, finding the optimal orientation which minimizes the coefficients for the first-order Zernike polynomials Z_1^1 and Z_1^{-1} , which model orientation of the sample about the x and y axes, as Supplementary Fig. 6b-f shows.

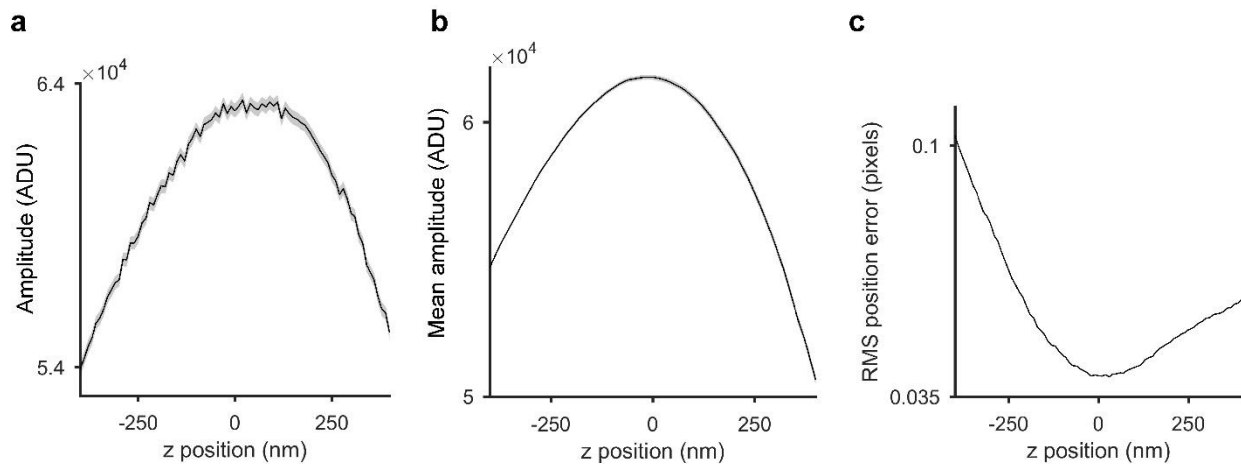


Supplementary Figure 6. Sample leveling. (a) Schematic showing sample holder. (b) Schematic showing sample orientation about the x axis, not to scale. (c) Plots showing correlation factor ρ at varying magnitudes of orientation about the x axis. Black dots indicate aperture positions. (d) Plots showing ρ at varying magnitudes of orientation about the y axis. Orientation direction corresponds to the schematics in (b). (e) Plot showing representative values of the coefficient for the Zernike polynomial Z_1^1 , modeling orientation about the x axis. The

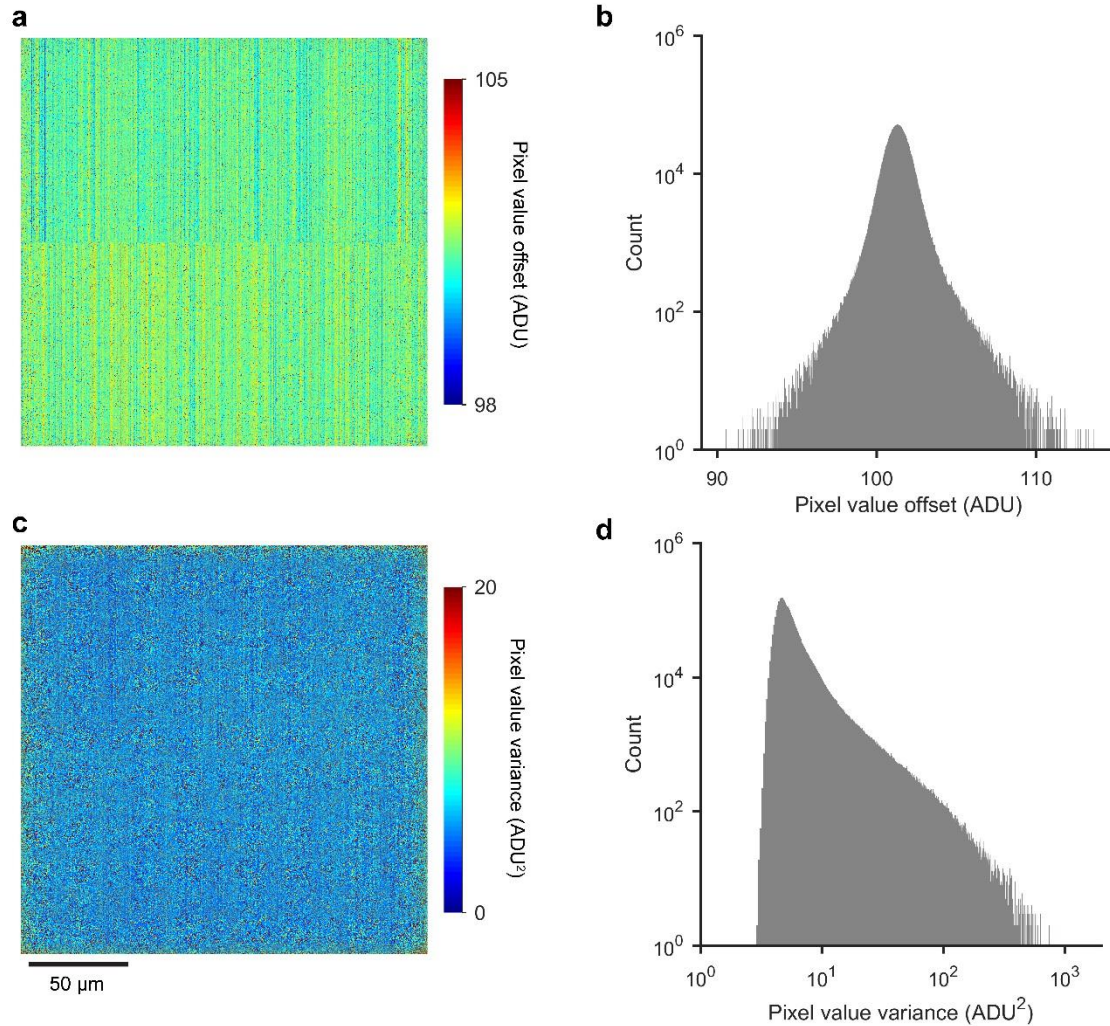
minimum corresponds to the center plot in (c). **(f)** Plot showing representative values of the coefficient for the Zernike polynomial Z_1^{-1} , modeling orientation about the y axis. The minimum corresponds to the center plot in (d).

Supplementary Note 4. Optimal focus

For any region of interest, from a single point spread function to the full field, we determine optimal focus first by imaging through focus. We then extract the mean amplitude of the point spread functions of interest, and empirically model the variation of this value with respect to z position using a quintic function. We take the maximum value of the model fit as the z position of optimal focus. Supplementary Fig. 7 shows amplitude as a function of z position for one aperture and mean amplitude as a function of z position for many apertures in one image.



Supplementary Figure 7. Optimal focus. **(a)** Plot showing the amplitude of the point spread function of a single aperture as a function of z position, with a maximum at optimal focus. The grey boundary is one standard deviation. **(b)** Plot showing the mean amplitude of 1600 point spread functions from as many apertures as a function of z position, with a maximum at optimal focus. The z positions of optimal focus differ between (a) and (b) due to field curvature. **(c)** Plot showing the mean error of a rigid transform between images of an aperture array as a function of z position, with a minimum at optimal focus. The grey boundaries in (b) and (c) are one standard error and are comparable in width to the black lines.



Supplementary Figure 8. Camera calibration. (a) Plot showing pixel value offset. (b) Histogram showing pixel value offset. (c) Plot showing pixel value variance. (d) Histogram showing pixel value variance. To clearly show systematic effects in (a) and (c) from the CMOS architecture of the imaging sensor, we restrict the ranges of (a) with respect to (b) and (c) with respect to (d).

Supplementary Note 5. CMOS localization

We develop a maximum-likelihood estimator to accurately localize single emitters over the full dynamic range and field of our CMOS camera. Our model for the response of each pixel is a Gaussian probability density function, which necessarily replaces the Poisson distribution that commonly models shot noise,^{20, 23-24} due to the nonlinear relationship between pixel value and total variance. The probability density function for each pixel incorporates the pixel value offset and flatfield correction factor in the calculation of the mean or expected pixel value to account for variation in pixel gain, illumination nonuniformity, and the effects of sensor packaging. The variance of the probability density function comes from the quartic function in the main text. To test this analysis, we perform Monte Carlo simulations to generate images of a univariate Gaussian point spread function in which this same Gaussian probability density function, incorporating parameter values that correspond exactly to a region of our CMOS camera,

determines each pixel value. Our analysis results in accurate localization with uncertainties near the Cramér–Rao lower bound, as Supplementary Table 2 shows. We find that using an approximate model for total variance, which includes only contributions from shot noise and read noise for each pixel, results in precision and accuracy that is equivalent to using the empirical model for the total variance. This demonstrates that, despite the difference between the empirical and approximate variance, which is significant for pixels with values in the top 25 % of the dynamic range, the approximate model is more computationally efficient and is sufficiently accurate even for data that spans the full dynamic range of the sensor.

Supplementary Table 2. CMOS localization

Photon count	Cramér–Rao lower bound (pixels)	x position standard deviation* (pixels)	x position standard error* (pixels)	x position error* (pixels)
4.5×10^5	2.7×10^{-3}	2.9×10^{-3}	4.1×10^{-5}	5.8×10^{-5}
7.0×10^5	2.2×10^{-3}	2.4×10^{-3}	3.4×10^{-5}	5.3×10^{-5}

*Values from measurements of 5000 images.

Supplementary Note 6. Fitting errors

A bivariate Gaussian model of the point spread function determines the expected pixel value in analog-to-digital units (ADU) for each pixel in an image,

$$E(x, y, FF, o, \Psi) = \frac{G_{biv}(x, y, \Psi) - o}{FF}, \quad (\text{Eq. S1})$$

where x and y are the position of the emitter in the image, o is the offset, FF is the flatfield correction factor, and G is a bivariate Gaussian function with parameter values Ψ ,

$$G_{biv}(x, y, \Psi = [A, \sigma_x, \sigma_y, \rho, C]) = A \cdot \exp - \left(\frac{1}{2(1-\rho^2)} \left[\frac{x^2}{\sigma_x^2} - 2\rho \frac{xy}{\sigma_x \sigma_y} + \frac{y^2}{\sigma_y^2} \right] \right) + C \quad (\text{Eq. S2})$$

The objective function for fitting this model of the expected values using weighted least-squares estimation is,

$$\hat{\Theta} = \operatorname{argmin} \left[\sum \frac{(I-E)^2}{I + \sigma_{read}^2} \right], \quad (\text{Eq. S3})$$

where $\hat{\Theta}$ is the estimate for the parameter set $\hat{\Theta} = \{A, \sigma_x, \sigma_y, \rho, x, y, C\}$, I is the experimental pixel value, E is the model or expected pixel value, and σ_{read}^2 is the read noise. In the case of a Gaussian probability density function for the response of single pixels, the objective function for maximum likelihood estimation is nearly identical,

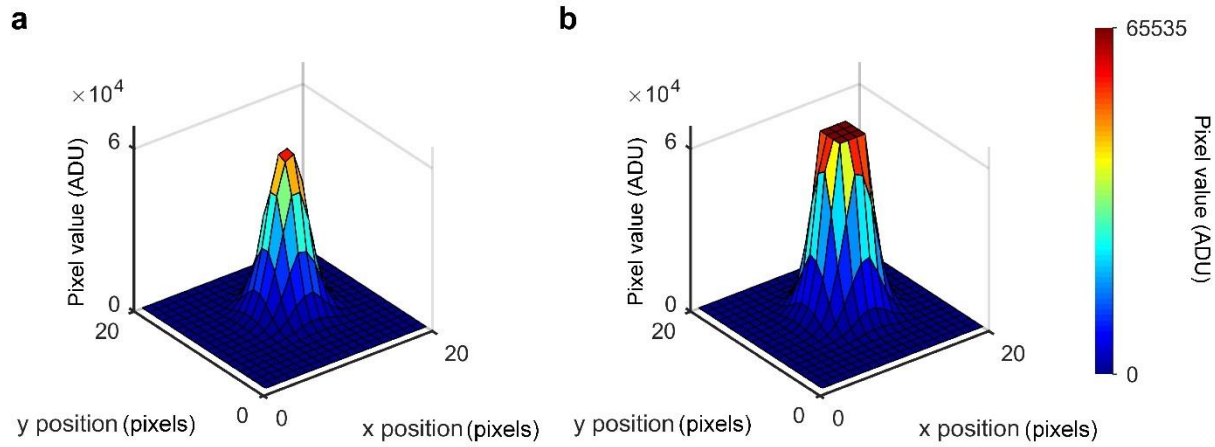
$$\hat{\Theta} = \operatorname{argmin} \left[\sum \frac{(I-E)^2}{E + \sigma_{read}^2} \right], \quad (\text{Eq. S4})$$

with the only difference being the replacement of the experimental pixel value I in the denominator of Eq. S3 with the model or expected pixel value E . If the model systematically underestimates the experimental pixel values, then the presence of the expected pixel value E in the denominator of Eq. S4 means that maximum-likelihood estimation gives additional weight to the underestimated pixel, as Fig. 4 shows. In contrast, the presence of I in the denominator of Eq. S3 means that weighted least-squares estimation does not have this bias. These effects are the opposite for the case that the model systematically overestimates the experimental values.

Here, we modify our localization algorithm to remove such effects. A general solution to this problem of choosing either weighted least-squares estimation or maximum-likelihood estimation is a hybrid objective function that reduces the potential for additional fitting errors regardless of whether the model systematically overestimates or underestimates the data,

$$\hat{\Theta} = \operatorname{argmin} \left[\sum \frac{(I-E)^2}{\max(I, E) + \sigma_{read}^2} \right], \quad (\text{Eq. S5})$$

where $\max(I, E)$ ensures the absence of incorrectly large weights for pixels where there is significant fitting error.



Supplementary Figure 9. Pixel saturation. Plots showing simulation results of a univariate Gaussian point spread function on a 16-bit imaging sensor. **(a)** The amplitude of the synthetic point spread function is below the saturation limit of the sensor. **(b)** The amplitude of the synthetic point spread function is above the saturation limit of the sensor.

Supplementary Note 7. Pixel saturation

We can modify our localization algorithm to account for pixel values with saturation,

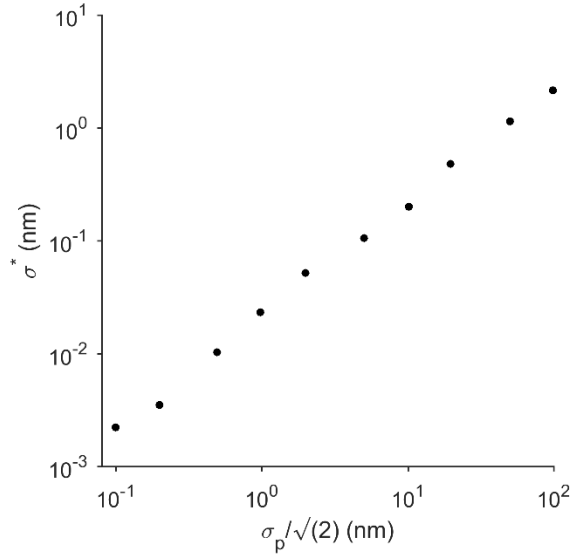
$$E_{sat} = \begin{cases} E & (I < I_{sat}) \\ I_{sat} & (I = I_{sat}) \end{cases}, \quad (\text{Eq. S6})$$

where I_{sat} is the maximum pixel value due to the bit depth of the imaging sensor. For our 16-bit sensor $I_{sat} = 65535$ ADU.

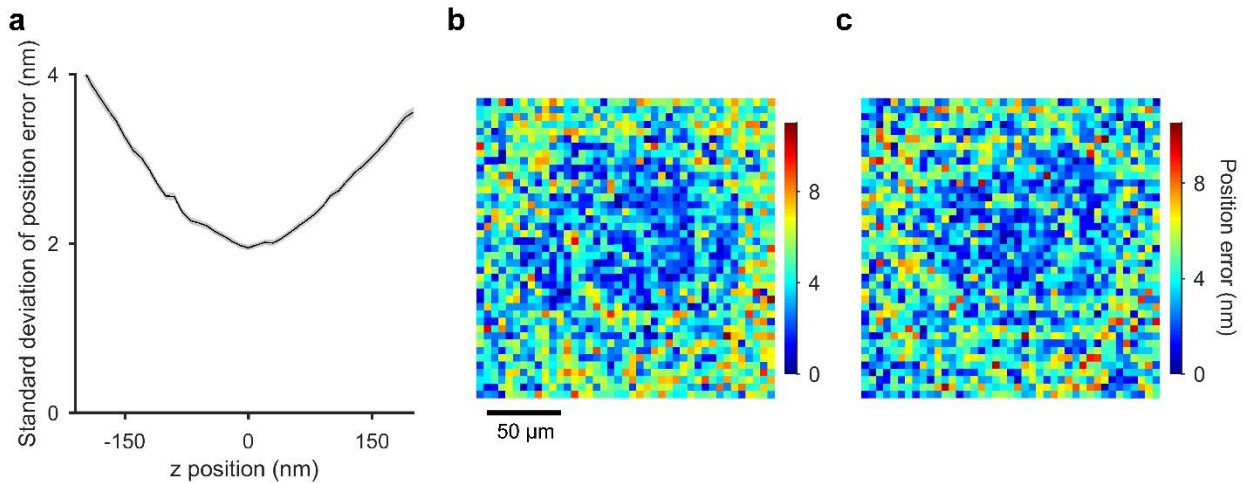
Supplementary Table 3. Pixel saturation

PSF amplitude (ADU)	x position standard deviation (pixels)	y position standard deviation (pixels)	x position error (pixels)	y position error (pixels)	Standard error of mean position (pixels)
< 65535	2.4×10^{-3}	2.4×10^{-3}	6.2×10^{-5}	5.6×10^{-5}	7.6×10^{-5}
> 65535 (MLE includes)	1.8×10^{-3}	1.7×10^{-3}	6.3×10^{-4}	1.1×10^{-3}	5.4×10^{-5}
> 65535 (MLE ignores)	1.8×10^{-3}	1.7×10^{-3}	3.6×10^{-4}	5.5×10^{-4}	5.4×10^{-5}

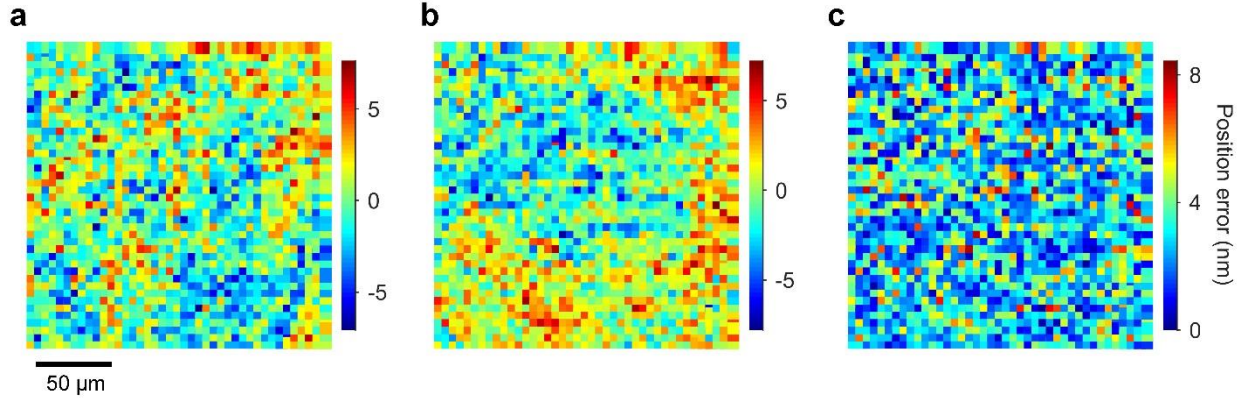
All values are from localization of 5000 synthetic point spread functions.



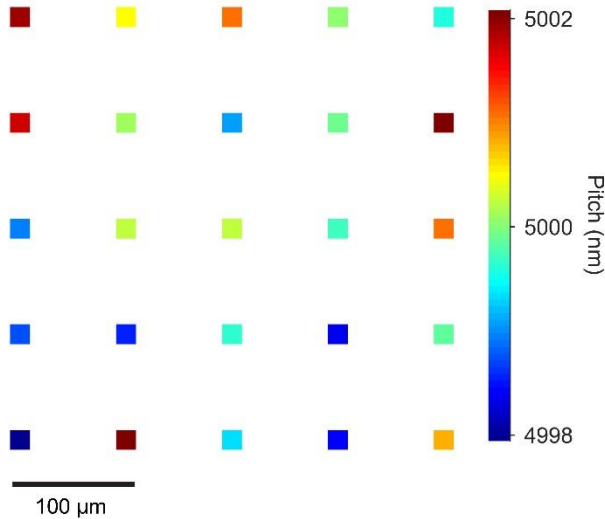
Supplementary Figure 10. Fabrication precision and error correction. Plot showing the amount of position error due to fabrication precision that the error correction model incorrectly captures, reducing its standard deviation by σ^* and contributing to widefield localization error. We perform a Monte Carlo simulation of $\sigma_p/\sqrt{2}$ as the standard deviation of a normal distribution around a mean pitch of 5 μm and apply the correction to the resulting aperture positions to determine σ^* , finding an approximately linear relation with small systematic deviations. σ^* is less than 0.05 nm for $\sigma_p/\sqrt{2} < 3$ nm, corresponding to our experimental aperture array. Standard errors of σ^* and $\sigma_p/\sqrt{2}$ for 1681 apertures are smaller than the data markers.



Supplementary Figure 11. Error is sensitive to focus. **(a)** Plot showing the pooled standard deviation of position errors in the x and y directions following error correction with respect to z position. The gray boundary is one standard error. **(b, c)** Plots showing the total magnitude of position errors at **(b)** 150 nm below the z position of optimal focus and **(c)** 150 nm above the z position of optimal focus. Position errors increase with z position, with a circular pattern around the center of the field. These position errors correspond to radial deformation of the field from defocus.



Supplementary Figure 12. Error correction across the array. Plots showing the magnitude of position errors in (a) the x direction, (b) the y direction, and (c) total from applying error correction models to the aperture positions from a different region of the array than in Section 3C. Systematic effects in (b) are consistent with focus variation with respect to the error maps in Fig. 6. Additional systematic effects that may indicate the presence of electron-optical aberrations are not apparent.



Supplementary Figure 13. Pitch across the aperture array. Plot showing 25 regions of the aperture array, with color scale indicating the mean pitch from four aperture pairs within each region. Data marker size is not to scale. No systematic effects indicative of electron-optical aberrations are evident.

Supplementary Note 8. Scanning and widefield measurements

The spatial variances of the pitch values that we measure using scanning and widefield measurements are, respectively,

$$\sigma_{\text{pitch},S}^2 = \sigma_{s,S}^2 + \sigma_p^2 + \sigma_{e,S}^2 \quad (\text{Eq. S6})$$

$$\sigma_{\text{pitch},W}^2 = \sigma_{s,W}^2 + \sigma_p^2 + \sigma_{e,W}^2 \quad (\text{Eq. S7})$$

where $\sigma_{s,S}^2$ is the variance from shot noise in scanning measurements, $\sigma_{s,W}^2$ is the variance from shot noise in widefield measurements, $\sigma_{e,S}^2$ is the variance from scanning measurement errors,

$\sigma_{e,W}^2$ is the variance from widefield measurement errors, and σ_p^2 is the variance from position errors due to fabrication precision. We determine the values of shot noise from the average variance of 1 600 pitch measurements over a time series of 100 images of the aperture array.

The variance of the distribution of the difference between corresponding pitch values from scanning and widefield measurements isolates the independent terms in σ_S^2 and σ_W^2 ,

$$\sigma_{S-W}^2 = \sigma_{s,S}^2 + \sigma_{s,W}^2 + \sigma_{e,W}^2 + \sigma_{e,S}^2, \quad (\text{Eq. S8})$$

and randomizing the correspondence between the scanning and widefield measurements of pitch causes σ_p^2 to be independent between the two measurement methods, giving a variance for the difference between the randomized pitch measurements of

$$(\sigma_{S-W}^2)_{\text{Random}} = \sigma_{s,S}^2 + \sigma_{s,W}^2 + \sigma_{e,W}^2 + \sigma_{e,S}^2 + 2\sigma_p^2. \quad (\text{Eq. S9})$$

Subtracting Eq. (S8) from Eq. (S9) isolates σ_p^2 , providing a measure of the position errors from fabrication precision that is free from shot noise and measurement errors. The associated standard deviations of aperture position error from fabrication precision are $\frac{\sigma_p}{\sqrt{2}}$, where the factor of $\frac{1}{\sqrt{2}}$ converts pitch error standard deviation to position error standard deviation. Supplementary Tables 4 and 5 give the values of all of the above quantities.

Inserting the values of σ_p^2 and $\sigma_{s,W}^2$ into Eq. (S7), we calculate a widefield position measurement error of $\frac{\sigma_{e,W}}{\sqrt{2}}$, for a purely random error. For a purely systematic error, the standard deviation of widefield measurements of pitch is

$$\sigma_W = \sqrt{\sigma_{s,W}^2 + \sigma_p^2} + \epsilon_W \quad (\text{Eq. S10})$$

where ϵ_W is a systematic error that adds arithmetically to the random and independent errors from shot noise and fabrication precision, giving a widefield position measurement error of $\frac{\epsilon_W}{\sqrt{2}}$.

Supplementary Table 5 gives the values of these widefield errors. We are not certain of the origin of this final error in our widefield measurements, or the extent to which it is random or systematic. Thus, $\frac{\epsilon_W}{\sqrt{2}}$ sets a lower limit and $\frac{\sigma_{e,W}}{\sqrt{2}}$ sets an upper limit on a range that quantifies our widefield localization error with appropriate uncertainty.

Values from an analogous analysis for scanning measurements of pitch are in Supplementary Table 4. These values and their components in Supplementary Table 5 are consistent with but slightly lower than the values in Table 1. This is due to small differences in the characterization of position error by either the ideal grid method or measurements of pitch, as well as the exclusion of shot noise.

The measurement uncertainties of variance values are the standard error of the variance as per Ref. 37 in the main text. To quantify values of σ_p , $\sigma_{e,W}$, and ϵ_W , we propagate uncertainties with either the NIST Uncertainty Machine, which is Ref. 38 in the main text, or the law of propagation of uncertainty.

Supplementary Table 4. Pitch variability

Measurement type	σ_{pitch}^2 (nm ²)	σ_s^{2*} (nm ²)	$\sigma_{e,\text{random}}^2$ (nm ²)	$\epsilon_{\text{systematic}}$ (nm)
x direction				
Widefield	6.83 ± 0.34**	0.184 ± 0.002**	0.78 ± 0.50***	0.15 ± 0.1***
Scanning	7.42 ± 0.37**	0.138 ± 0.0006**	1.41 ± 0.52***	0.27 ± 0.1***
y direction				
Widefield	7.73 ± 0.39**	0.154 ± 0.001**	1.03 ± 0.54***	0.19 ± 0.1***
Scanning	7.25 ± 0.36**	0.131 ± 0.0006**	0.57 ± 0.52***	0.11 ± 0.1***

*Mean variance of 800 values of pitch from a series of 100 images

**Standard error

***NIST uncertainty machine

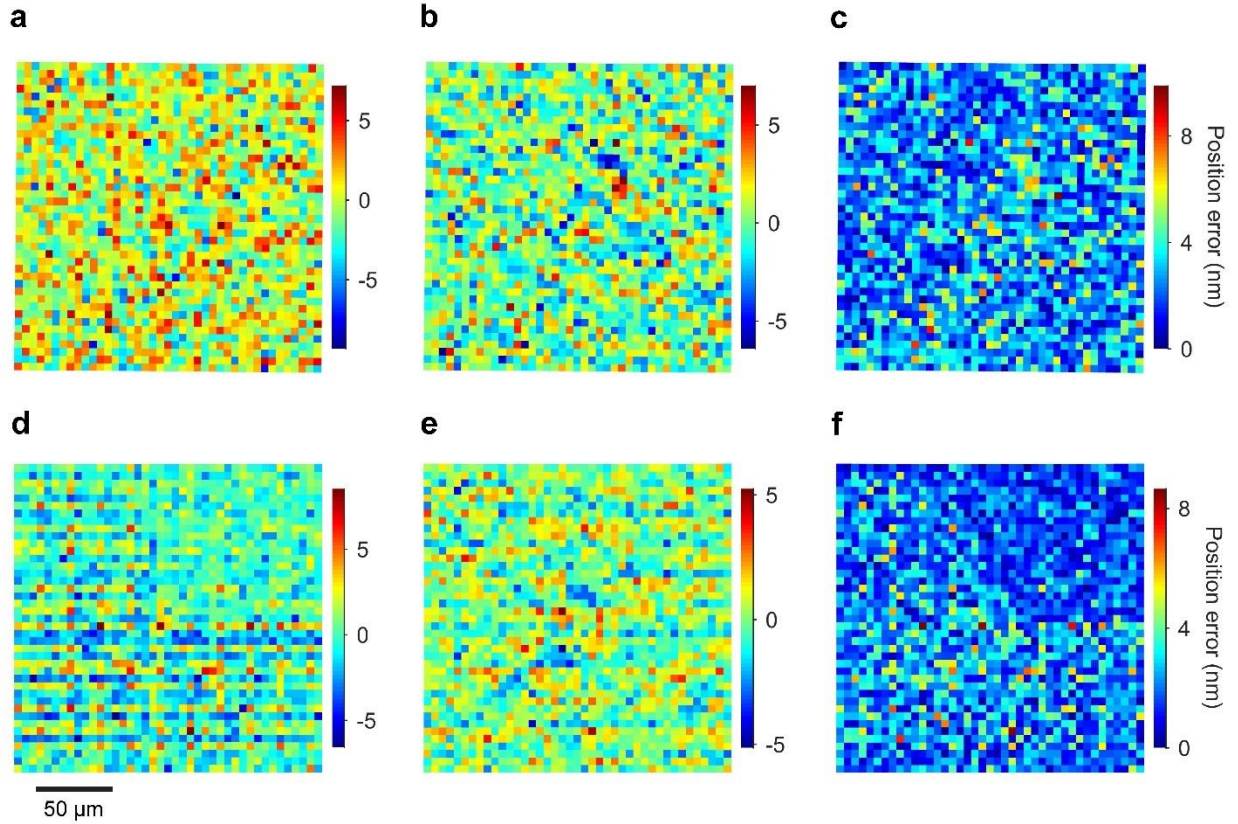
Supplementary Table 5. From pitch variance to position standard deviation

Quantity	x direction	y direction
σ_{s-w}^2 (nm ²)	2.51 ± 0.13*	1.88 ± 0.09*
$(\sigma_{s-w}^2)_{\text{Random}}$ (nm ²)	14.25 ± 0.71*	14.98 ± 0.75*
σ_p^2 (nm ²)	5.87 ± 0.36**	6.55 ± 0.38**
$\sigma_p/\sqrt{2}$ (nm)	1.71 ± 0.05**	1.81 ± 0.05**
$\sigma_{e,w}/\sqrt{2}$ (random) (nm)	0.62 ± 0.20***	0.72 ± 0.19***
$\epsilon_{e,w}/\sqrt{2}$ (systematic) (nm)	0.11 ± 0.07***	0.13 ± 0.07***

*Standard error

**NIST uncertainty machine

***Propagation of uncertainty



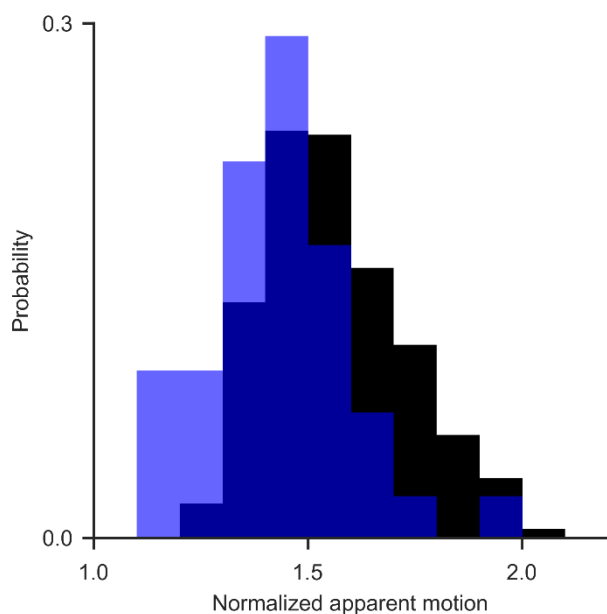
Supplementary Figure 14. Patterning processes. **(a-c)** Plots showing the magnitude of position errors in (a) the x direction, (b) the y direction, and (c) total that are the result of applying error correction models to measurements of aperture positions from an array that we pattern by decreasing the electron-beam current from 1.0 nA to 0.2 nA and increasing the dwell time proportionately to deliver the same dose. **(d-f)** Maps showing the magnitude of position errors in (d) the x direction, (e) the y direction, and (f) total that are the result of applying error correction models to measurements of aperture positions from an array that we pattern by decreasing the electron-beam current from 1.0 nA to 0.125 nA, maintaining the dwell time, and taking eight passes to deliver the same dose. Systematic errors from pattern overwriting are apparent as horizontal stripes. The upper right quadrant of (d) and (f) shows systematically lower values of position error, indicating an interesting irregularity of the patterning process in this instance.

Supplementary Note 9. Rigidity analysis

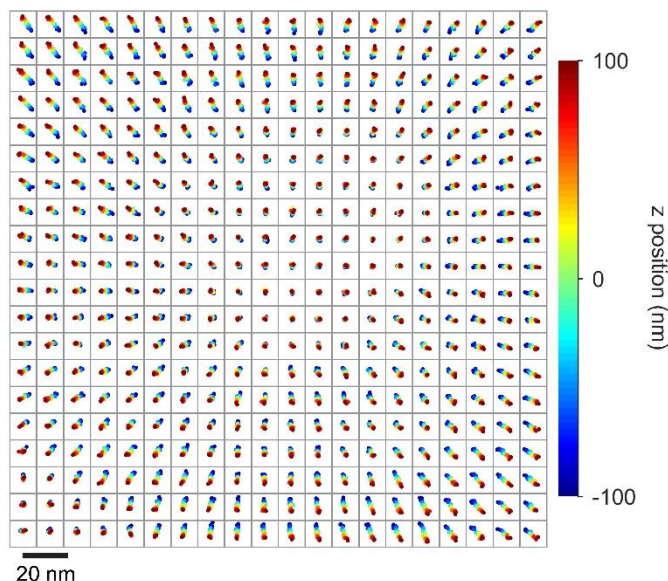
The positions of each aperture or nanoparticle define a nominally rigid constellation of points in the image plane, $(x_{j,\eta}, y_{j,\eta})$, where the index j denotes an image in a measurement series and the index η denotes the position of a point in a constellation³. We measure the common-mode motion of the sample by applying a two-dimensional rigid transformation to map the constellation in image j to the constellation in image k . This transformation consists of a displacement of the centroid of the constellation $(X_j - X_k) \hat{x} + (Y_j - Y_k) \hat{y}$ and a rotation of the constellation about the centroid, $\Delta\theta = \theta_j - \theta_k$, where (X_j, Y_j) and (X_k, Y_k) are the positions of the centroids in images j and k , respectively, and θ_j and θ_k are the orientations of the constellation in images j and k , respectively. The optimal rigid transformation minimizes the root-mean-square distance, or error, between corresponding points in images j and k . Such error

is insensitive to systematic error in localizing single apertures or nanoparticles. Therefore, this rigidity analysis does not require calibration of pixel read noise, which we omit.

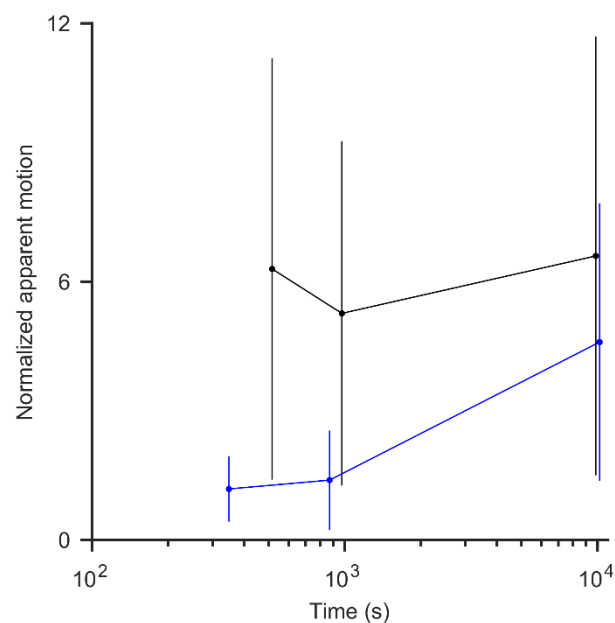
Motion of a sample in z during a time series can cause apparent deformation of a rigid constellation in optical micrographs. We minimize these effects by imaging through focus at each point in the time series, acquiring images at multiple positions in z around the common focal plane for the entire time series. The nominal spacing in z between each image is 10 nm, set by the resolution of our piezoelectric nosepiece that controls the position of the objective lens. We then choose the image that minimizes the root-mean-square error of the rigid transformation of the constellation with respect to that from the first image in the time series. This procedure minimizes any motion of the sample in z relative to the position at the initial time point, so that the images that form the resulting time series share a common focal plane within 10 nm.



Supplementary Figure 15. Nanoparticle stability down to 10^{-1} s. Plot showing probability distributions of normalized apparent motion for nominally motionless apertures (black) and nanoparticles (blue) that we image at a frequency of 10^1 s $^{-1}$ for a duration of 10^1 s, without intentionally changing the z position. We quantify apparent motion by the root-mean-square error of a rigid transform between pairs of consecutive images. The normalization is with respect to the Cramér–Rao lower bound and accounts primarily for differences in the number of signal photons. The corresponding absolute mean values define the measurement uncertainties, and are approximately 0.43 nm for apertures and 0.55 nm for nanoparticles. The magnitude of normalized apparent motion for nanoparticles is comparable to that of static apertures, indicating that the nanoparticles are also static at these scales.



Supplementary Figure 16. Apparent motion. Grid of scatterplots, each corresponding to a single aperture, showing apparent motion in the radial direction due to imaging through focus over a range of 200 nm in z position. The grid spacing indicates an aperture array pitch of 10 μm . The scale bar corresponds to the scatterplots.



Supplementary Figure 17. Nanoparticle stability up to 10^4 s. Plot showing normalized apparent motion as a function of time, exceeding the time that is necessary for imaging through focus, for nominally static apertures (black) and nanoparticles (blue). Normalization is with respect to measurement uncertainty, or the corresponding values of apparent motion at the time scale of 10^{-1} s. Data markers are mean values and vertical bars are \pm one standard deviation. The values of normalized apparent motion for nanoparticles are comparable to those of apertures, indicating that the nanoparticles are static at these scales.